







ARTICLE

Structures of the fungal dynamin-related protein Vps1 reveal a unique, open helical architecture

Natalia V. Varlakhanova^{1*} , Frances J.D. Alvarez^{2*} , Tyler M. Brady¹, Bryan A. Tornabene¹, Christopher J. Hosford³ , Joshua S. Chappie³ ,
Peijun Zhang^{2,4,5} , and Marijn G.J. Ford¹ 

Dynamin-related proteins (DRPs) are large multidomain GTPases required for diverse membrane-remodeling events. DRPs self-assemble into helical structures, but how these structures are tailored to their cellular targets remains unclear. We demonstrate that the fungal DRP Vps1 primarily localizes to and functions at the endosomal compartment. We present crystal structures of a Vps1 GTPase–bundle signaling element (BSE) fusion in different nucleotide states to capture GTP hydrolysis intermediates and concomitant conformational changes. Using cryoEM, we determined the structure of full-length GMPPCP-bound Vps1. The Vps1 helix is more open and flexible than that of dynamin. This is due to further opening of the BSEs away from the GTPase domains. A novel interface between adjacent GTPase domains forms in Vps1 instead of the contacts between the BSE and adjacent stalks and GTPase domains as seen in dynamin. Disruption of this interface abolishes Vps1 function in vivo. Hence, Vps1 exhibits a unique helical architecture, highlighting structural flexibilities of DRP self-assembly.

Introduction

Dynamin-related proteins (DRPs) are large multidomain GTPases that play central roles in membrane fission and fusion events throughout the cell (Praefcke and McMahon, 2004; Hoppins et al., 2007; Ferguson and De Camilli, 2012). DRPs are vital for many cellular functions that depend on membrane remodeling including endocytosis, intracellular trafficking, mitochondrial dynamics, and energy homeostasis. Mutations in DRPs are associated with aging as well as several human diseases including neurodegeneration, optic atrophy, and Charcot Marie Tooth type 2A (Faelber et al., 2013).

All DRPs remodel membranes using a similar general mechanism: coordinated self-assembly coupled with GTP hydrolysis-dependent conformational changes (Chappie and Dyda, 2013; Antonny et al., 2016). The general mechanism of action of DRPs has been extensively studied for both fission DRPs such as dynamin and fusion DRPs such as Mfn1/Fzo1 as well as more distant members of the family including the bacterial dynamin-like proteins, Mx proteins, and atlastins (Low and Löwe, 2006; Low et al., 2009; Chappie et al., 2010, 2011; Bian et al., 2011; Byrnes and Sonderrmann, 2011; Faelber et al., 2011; Ford et al., 2011; Gao et al., 2011; Byrnes et al., 2013; Fröhlich et al., 2013; Reubold et al., 2015; Qi et al., 2016; Alvarez et al., 2017; Cao et al., 2017; Francy et al., 2017). Due to the functional versatility of DRPs and their ubiquity

within cellular environments, considerable interest exists in understanding how specific DRPs are tailored for their particular functional niche and cellular targets.

Vps1 is a conserved fungal DRP that was originally identified in screens designed to capture mutants that are deficient in sorting of carboxypeptidase Y (CPY) to the vacuole (Rothman and Stevens, 1986; Vater et al., 1992). $\Delta vps1$ cells exhibit major defects in vacuolar dynamics and cargo transport to the vacuole (Raymond et al., 1992). Vps1 has been implicated in both vacuolar fusion and fission (Peters et al., 2004) as well as in regulation of peroxisome abundance and division, late endosome-to-vacuole trafficking, endocytosis, and retrograde trafficking from the endosomes and vacuoles (Kuravi et al., 2006; Smaczynska-de Rooij et al., 2010, 2012; Hayden et al., 2013; Chi et al., 2014; Arlt et al., 2015). Despite the clear importance of Vps1 for regulating fundamental yeast cellular processes, no structural analysis of Vps1 has been reported to date.

By sequence homology, Vps1 shares three structural domains with dynamin I: a catalytic GTPase domain, a three-helix bundle termed the bundle signaling element (BSE), and an all-helical Stalk formed by three helices from the Middle domain and one from the GTPase Effector Domain (GED; Fig. 1; Chappie and Dyda, 2013). The BSE, formed by two helices that flank the GTPase and

¹Department of Cell Biology, University of Pittsburgh School of Medicine, Pittsburgh, PA; ²Department of Structural Biology, University of Pittsburgh School of Medicine, Pittsburgh, PA; ³Department of Molecular Medicine, Cornell University, Ithaca, NY; ⁴Division of Structural Biology, Wellcome Trust Centre for Human Genetics, University of Oxford, Oxford, UK; ⁵Electron Bio-Imaging Centre, Diamond Light Source, Harwell Science and Innovation Campus, Didcot, UK.

*N.V. Varlakhanova and F.J.D. Alvarez contributed equally to this paper; Correspondence to Marijn G.J. Ford: marijn@pitt.edu.

© 2018 Varlakhanova et al. This article is distributed under the terms of an Attribution–Noncommercial–Share Alike–No Mirror Sites license for the first six months after the publication date (see <http://www.rupress.org/terms/>). After six months it is available under a Creative Commons License (Attribution–Noncommercial–Share Alike 4.0 International license, as described at <https://creativecommons.org/licenses/by-nc-sa/4.0/>).

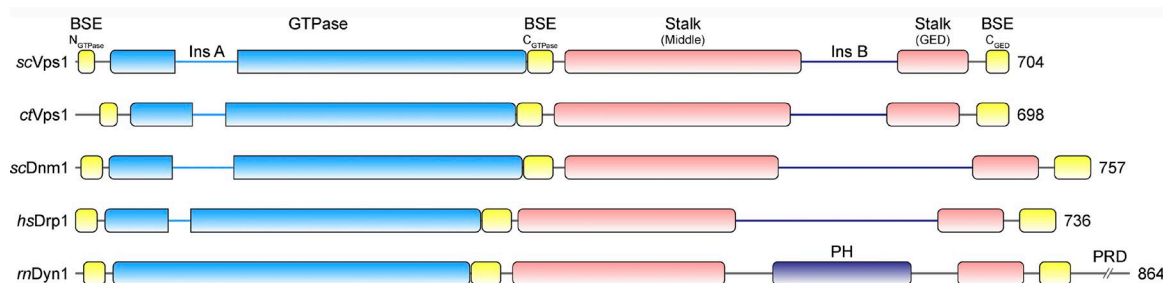


Figure 1. **Domain architecture of Vps1.** Schematic of the domain structures of Vps1 and select other DRPs. Domain coloration shown in this figure is used throughout this study. The Stalk is a composite domain consisting of Middle and GED. *sc*, *S. cerevisiae*; *ct*, *C. thermophilum*; *hs*, *H. sapiens*; *m*, *Rattus norvegicus*; InsA, Insert A; InsB, Insert B. The lengths of the sequences are shown to the right of the schematics.

a helix from the C-terminal part of GED, is an intramolecular signaling module that transmits hydrolysis-dependent conformational changes from the GTPase domain to the rest of the molecule, while the Stalk mediates self-assembly and higher-order oligomerization (Gao et al., 2010, 2011; Faelber et al., 2011; Ford et al., 2011). Dynamin, uniquely, has a pleckstrin homology (PH) domain between its middle and GED as well as a C-terminal proline- and arginine-rich domain (PRD). The dynamin PH domain preferentially interacts with membranes containing phosphatidylinositol-(4,5)-bisphosphate and plays a critical function in membrane recruitment, regulation of self-assembly, and, by penetrating the membrane, fission (Achiriloae et al., 1999; Ramachandran et al., 2009; Kenniston and Lemmon, 2010). The PRD contains numerous interaction motifs for multiple binding partners and is required for dynamin recruitment to its sites of action. Vps1 lacks both a PH and a PRD. These differences, therefore, necessitate alternative membrane recruitment mechanisms for Vps1. Vps1 and other non-dynamin DRPs have two features absent in dynamin: Insert A and Insert B. Insert A is an insertion of 25–50 residues of unknown function within the GTPase domain. Insert B is a stretch of ~75 nonconserved residues that replaces the PH and is predicted to be of low complexity. How these Vps1 features affect its structure and function remains unclear.

To address these outstanding questions, we performed an extensive functional, biochemical, and structural characterization of Vps1. We show that Vps1 preferentially associates with the endosomal compartment and is required for its dynamics and morphology. We crystallized minimal GTPase-BSE fusion constructs of Vps1 in different nucleotide states to capture intermediates of the Vps1 GTP hydrolysis cycle. We show via cryoEM that Vps1 self-assembles into helices that are more flexible and fenestrated than those generated by dynamin. Using a pseudoatomic model generated by combining our crystal structures with our reconstruction of the Vps1 helical assembly, we identified a novel interface between adjacent GTPase domains. Disruption of this interface abrogates Vps1 function in vivo. Furthermore, the Vps1 helical assembly lacks the lateral contacts between its BSEs and adjacent GTPases and Stalks that are observed in pseudoatomic models of the dynamin assembly. These structural adaptations contribute to the more open helical architecture of Vps1 and may help Vps1 to remodel a wider range of potential templates. Collectively, our data reveal specific structural adaptations to the basic DRP machine that accommodate its unique functional requirements.

Results

Vps1 localizes to and functions at the endosomal compartment

Cells lacking Vps1 ($\Delta vps1$) exhibited altered vacuolar morphology and dynamics when compared with WT cells (strain W303A; Fig. S1 A and Videos 1 and 2; Raymond et al., 1992; Peters et al., 2004) as assessed by visualizing the vacuolar membrane using either the lipophilic dye FM 4–64 (Vida and Emr, 1995) or by using genomically-integrated EGFP-tagged vacuolar membrane protein Vph1. W303A cells had dynamic and flexible vacuoles that frequently exhibited fusion and fission events. By contrast, the vacuolar compartment in $\Delta vps1$ cells consisted of static spherical components that were often clustered (Videos 1 and 2). $\Delta vps1$ cells also exhibited significant defects in endosomal function and morphology (Hayden et al., 2013; Lukehart et al., 2013). Snc1 is a v-SNARE required for fusion of vesicles from the TGN with the plasma membrane but is itself recycled via the endosomal compartment (Lewis et al., 2000). Steady-state localization of Snc1 was disrupted in $\Delta vps1$ cells: Snc1 was mislocalized to the vacuolar membrane, whereas in WT cells, it was primarily found on the plasma membrane (Fig. S1 B; Saimani et al., 2017). In WT cells, Tlg2, a t-SNARE used as a late endosomal marker, was punctate throughout the cytosol, whereas in $\Delta vps1$ cells, Tlg2 was mislocalized to the vacuolar membrane (Fig. S1 C). Remaining Tlg2 puncta appeared to be associated with the vacuolar membrane.

The endosomal compartment is enriched in phosphatidylinositol 3-phosphate (PI3P; Gillooly et al., 2000). Some PI3P is also found on the vacuolar membrane and is particularly enriched at the vertex junctions of docked vacuoles, where it plays an important role in vacuolar fusion (Fratti et al., 2004). We examined the localization of PI3P in WT and $\Delta vps1$ cells using the GFP-tagged FYVE domain from mammalian EEA1 as a probe (Burd and Emr, 1998). We observed highly dynamic FYVE puncta in WT cells (Fig. 2 A and Video 3). A diffuse FYVE signal was also detected throughout the vacuolar membrane. In $\Delta vps1$ cells, the PI3P signal lost its dynamic nature and was enriched to the cluster adjacent to the vacuole, representing the defective endosomal compartment (Fig. 2 A and Video 4).

Some aspects of endosomal function did not appear to be disrupted in $\Delta vps1$ cells. The multivesicular body (MVB) biogenesis pathway was intact in $\Delta vps1$ cells, as determined by examining the localization of carboxypeptidase S tagged with EGFP (Cps1-EGFP; Fig. S1 D). Cps1-EGFP did not accumulate in the endosomal compartment in $\Delta vps1$ cells, whereas it did in cells lacking Vps4,

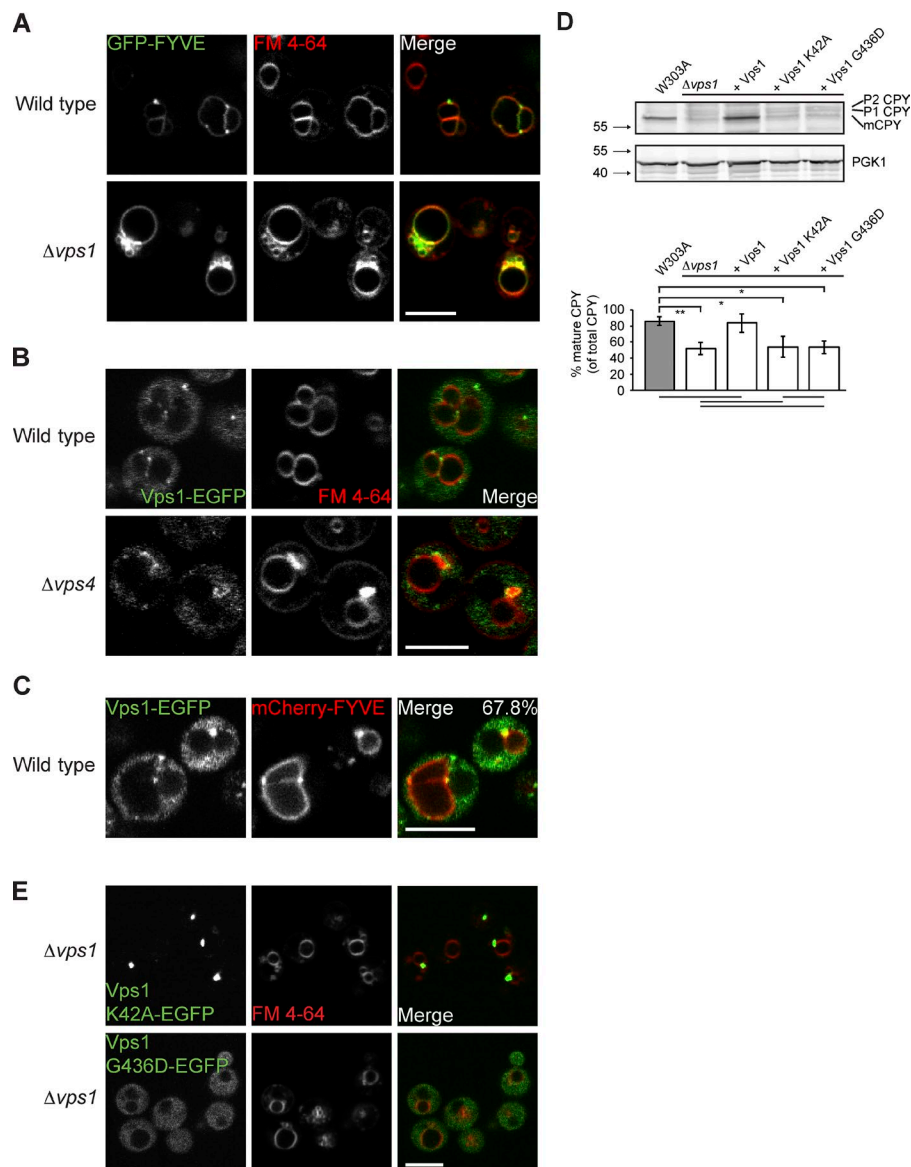


Figure 2. Cells lacking Vps1 are defective in vacuolar and endosomal morphology and trafficking. (A) WT (W303A) and $\Delta vps1$ cells expressing GFP-FYVE were stained with FM 4-64 and were visualized by confocal microscopy. (B) WT and $\Delta vps4$ cells expressing Vps1-EGFP were stained with FM 4-64. (C) Visualization of WT cells expressing Vps1-EGFP and mCherry-FYVE. Vps1 puncta partially colocalized with FYVE puncta ($67.8 \pm 4.9\%$). (D) CPY maturation in $\Delta vps1$ cells. mCPY is the mature form, and P1 and P2 are intermediates. PGK1 is the loading control. The ratio of mature to total CPY was determined for each sample ($n = 3$). The means of the ratios of mature to total CPY were significantly heterogeneous (one-way ANOVA, $F_{4,10} = 10.1$; $P = 0.002$). A Tukey-Kramer post hoc test was used to assess the significance of differences between means: those not significantly different from one another are indicated below the graph ($P > 0.05$), whereas selected pairs of means that are significantly different are indicated above the graph: *, $P < 0.05$; **, $P < 0.01$. Molecular masses are given in kilodaltons. (E) Visualization of cells expressing the indicated Vps1 mutant. Bars, 5 μ m.

which is known to cause a defect in MVB biogenesis (Fig. S1 D; Shestakova et al., 2010).

Vps1 tagged with EGFP using a linker customized to include a stretch of 10 asparagine residues was fully functional and rescued the known growth defect of $\Delta vps1$ cells at 37°C (Fig. S2 A; Rothman et al., 1990). Vps1 generally had a diffuse cytosolic localization with highly dynamic foci that concentrated at vacuolar vertex junctions (Fig. 2 B). Deletion of Vps4, which is required for disassembly of ESCRT-III filaments and therefore proper endosomal function (Schöneberg et al., 2017), resulted in the expected Class E morphology of the endosomal compartment, with endosomes extensively stacked together adjacent to the vacuole (Babst et al., 1997; Finken-Eigen et al., 1997). In $\Delta vps4$ cells, Vps1 clustered around the class E compartment (Fig. 2 B). Furthermore, we observed significant endosomal localization for Vps1 based on colocalization with endosomal puncta labeled with FYVE (Fig. 2 C). $67.8 \pm 4.9\%$ of Vps1 puncta were associated with PI3P puncta ($n = 181$). We also observed some Vps1 enrichment within developing buds that was not associated with PI3P (not

depicted). Taken together, these data indicate that Vps1 primarily concentrates within the endosomal compartment.

Self-assembly and coordinated GTP hydrolysis are necessary for the function of other DRPs. Stalk mutants, such as G397D in rat dynamin 1 and G385D in Dnm1, are defective in self-assembly and impair function (Ingberman et al., 2005; Ford et al., 2011). Mutants like K44A in human dynamin 1 lack efficient catalytic turnover and act as dominant negatives in vivo, trapping the helical assembly in a hyperconstricted pre-fission state (Damke et al., 1994; Sundborger et al., 2014). To determine the effect of Vps1 oligomerization and hydrolysis on endosomal function, we introduced point mutations into Vps1 at analogous positions (G436D and K42A). Vps1 G436D produced stable dimers in solution as assessed by size-exclusion chromatography (SEC) coupled to multiangle light scattering (MALS; SEC-MALS; Fig. S2 B). Like all other vps mutants, Vps1 is required for trafficking and maturation of CPY (Stevens et al., 1982). Cells lacking Vps1 exhibited a defect in maturation of CPY (Fig. 2 D). Expression of WT Vps1 in $\Delta vps1$ cells fully rescued this defect, whereas expression of either Vps1 K42A or Vps1 G436D did

not. When tagged with EGFP, all expressed Vps1 K42A appeared to concentrate in defined intense spots adjacent to the vacuole (Fig. 2 E). The Vps1 K42A puncta formed at endosomal sites based on colocalization with those formed by mCherry-FYVE (Fig. S2 C). Strikingly, overexpression of Vps1 K42A in $\Delta vps1$ cells resulted in formation of extended filaments that appeared tangentially attached to the vacuolar compartment (Fig. S2 D). By contrast, Vps1 G436D-EGFP was diffuse and did not form puncta (Figs. 2 E and S2 C) as expected for a higher-order assembly-deficient DRP. $\Delta vps1$ cells expressing either mutant retained the vacuolar morphology observed in $\Delta vps1$ cells (Fig. 2 E). Expression levels for Vps1-EGFP and Vps1 K42A-EGFP in $\Delta vps1$ cells were comparable, while levels for Vps1 G436D-EGFP were slightly elevated (Fig. S2 E). Hence, the defects observed were not due to variations in expression levels of the mutants. When Vps1 K42A was overexpressed in WT cells, the vacuolar morphology seen in $\Delta vps1$ cells was induced (Fig. S2 F). By contrast, overexpression of Vps1 G436D in WT cells did not exhibit a dominant-negative phenotype. These data indicate Vps1 has a major endosomal function that depends on Vps1 assembly and hydrolysis.

Biochemical characterization of Vps1

As attempts to purify *Saccharomyces cerevisiae* Vps1 were unsuccessful, we sought an alternative source of Vps1 that was more amenable to purification and characterization. We therefore screened other fungal *VPS1* genes for the ability to rescue the growth defect of $\Delta vps1$ cells at 37°C. *VPS1* from *Chaetomium thermophilum* fully rescued the $\Delta vps1$ phenotype (Fig. 3 A). We purified *C. thermophilum* Vps1 fused to maltose-binding protein (MBP) after transient expression in Expi293F cells. The protein exhibited GTP hydrolysis with a basal activity of 1.52 hydrolysis events per minute, comparable with that observed for rat dynamin 1 (3.05 min⁻¹; Fig. S3 A). The presence of dioleoyl phosphatidyl serine (DOPS) liposomes minimally stimulated Vps1 (3.05 min⁻¹), while dynamin 1 was robustly stimulated to a turnover of 41.3 min⁻¹ (Fig. S3 A; Warnock et al., 1995; Stowell et al., 1999; Ford et al., 2011). Removal of the MBP tag did not significantly alter these rates (no liposomes, 2.0 min⁻¹; DOPS, 3.3 min⁻¹; Fig. S3 B and not depicted). Substitution of lipid nanotubes containing phosphoserine (PS) and PI3P for DOPS liposomes similarly showed only minimal stimulation of Vps1 GTPase activity (absence, 2.0 min⁻¹; presence, 3.6 min⁻¹), whereas dynamin 1 was again robustly stimulated (presence, 39.6 min⁻¹; not depicted). Vps1 was, however, able to assemble into helical structures on these nanotubes (Fig. 3 B). Hence, the absence of significant lipid stimulation of GTP hydrolysis by Vps1 is not due to an inability of Vps1 to self-assemble on lipid templates.

We next purified and characterized the hydrolysis of a minimal GTPase-BSE construct from *C. thermophilum* Vps1 (hereafter Vps1 GG), comparable with the minimal GG construct previously used for dynamin 1 (Chappie et al., 2009, 2010, 2011). Dynamin 1 GG dimerizes in the presence of GDP·AlF₄⁻, and this change can be monitored by SEC (Fig. S3 C; Chappie et al., 2010). Vps1 GG only exhibited a shift to a faster-migrating species on SEC with GDP·AlF₄⁻ but not when preincubated with GMPPCP, GTPγS, or GDP (Fig. S3 D). SEC-MALS confirmed that Vps1 GG dimerized only in the presence of GDP·AlF₄⁻ (Fig. 3 C). Vps1 GG exhibited

basal GTPase activity of 1.1 min⁻¹ with an apparent K_M of 60 μM, as assessed using a colorimetric phosphate release assay (Fig. 3 D; Leonard et al., 2005). This hydrolysis activity was not stimulated by DOPS liposomes (not depicted). Since GTP hydrolysis by rat full-length dynamin 1 is robustly stimulated by liposomes (Fig. S3 A), assembly is required for GTP hydrolysis (especially stimulated hydrolysis). Full-length Vps1 assembled (see above) but exhibited only modest lipid-stimulated GTP hydrolysis. This difference in stimulated GTP hydrolysis rates may allow Vps1 to assemble into longer and more persistent structures.

The crystal structures of Vps1 GG bound to GMPPCP, GDP·AlF₄⁻, and GDP

To characterize the catalytic cycle of Vps1, we crystallized Vps1 GG in complex with GMPPCP, GDP·AlF₄⁻, and GDP, respectively (Figs. 4 and S4 A). Vps1 GG in complex with GMPPCP (hereafter GG_{GMPPCP}) crystallized with two complete nucleotide-bound GG dimers in the asymmetric unit, which superposed with root mean square (r.m.s.) deviations of Cα residues of 0.55 Å; Fig. S4 B). The dimers were formed by the GMPPCP-bound GTPase domains and buried a surface area of 2,486 Å² (Fig. 4 A). Each GTPase bound one GMPPCP in a deep pocket (Fig. 4 B) that was closed off at the dimer interface by the other monomer. In the binding pocket, an Mg²⁺ ion was coordinated by the side-chain hydroxyl groups of Ser57 in the P loop and Thr77 in Switch 1 as well as the β- and γ-phosphates of the nucleotide. The β-phosphate also formed a hydrogen bond with the side chain of Lys56. The guanosine base was coordinated by the side chain of Asp242 in G4 and was also contacted in trans by the side chain of Asp245 from the G4 loop of the dimer partner. Switches 1 and 2 were also both well ordered (Fig. 4 C). The BSEs in this structure were in the fully extended open conformation (Fig. 4 A). However, the close approach of neighboring molecules related by noncrystallographic symmetry induced local disorder in the C_{GED} helix of the BSE of molecule D (Fig. S4 B). Consequently, the structural model for this BSE was less complete.

Vps1 GG in complex with GDP·AlF₄⁻ (GG_{GDP·AlF₄⁻}; Fig. 4 D) also crystallized with two complete GG dimers in the asymmetric unit, which superposed with r.m.s. deviations of Cα residues: 0.68 Å (Fig. S4 C). The GTPases formed the same canonical interface with an inaccessible area of 2,586 Å². We observed density for GDP, AlF₄⁻, along with an additional density peak that was coordinated by the side chain of Ser43 in the P loop, the main chain carbonyl oxygens of Gly72 and Gly74 at the top of Switch 1, a β-phosphate oxygen, and a fluorine within the AlF₄⁻ moiety. We interpret this density as a sodium ion based on the presence of a sodium ion in the equivalent position of the dynamin 1 GG structure in complex with GDP·AlF₄⁻ (Fig. 4, E and F; Chappie et al., 2010). Surprisingly, the BSEs in this structure were also in the fully extended, open conformation (Fig. 4 D). As for GG_{GMPPCP}, the C_{GED} helix of molecule D was disordered (Fig. S4 C).

Both GG_{GMPPCP} and GG_{GDP·AlF₄⁻} structures had additional interpretable density N-terminal to the N_{GTPase} helix. *C. thermophilum* Vps1 has a unique N-terminal extension of 19 amino acids. This packs against the core of the GTPase domain (Fig. S4 D). The function of this extension remains unknown, but its presence is required to produce abundant soluble protein.

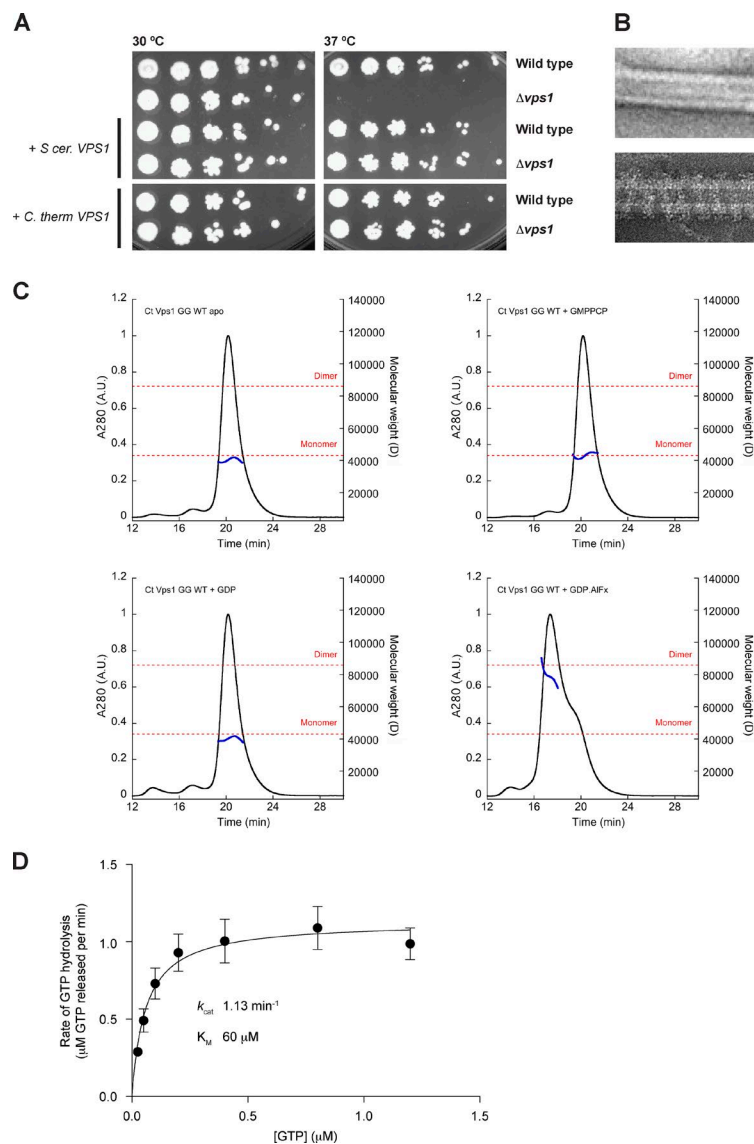


Figure 3. In vitro characterization of full-length *C. thermophilum* Vps1 and a minimal Vps1 GG construct. (A) Growth of WT (W303A) or $\Delta vps1$ cells expressing the indicated constructs on YPD plates at 30 or 37°C. The leftmost spot in each case corresponds with 2 μ l of a culture of OD₆₀₀ 0.5. Spots to the right of this correspond with 2 μ l sequential fivefold dilutions. (B) Lipid nanotubes containing 40% DOPS and 20% PI3P were incubated with *C. thermophilum* Vps1 before staining and imaging. Top: Naked nanotube. Bottom: Nanotube decorated with Vps1. Bar, 50 nm. (C) Molecular weight determination of *C. thermophilum* Vps1 GG. Absolute molecular weights (shown in blue across the elution peaks and plotted on the right-hand axes) were determined using SEC-MALS. Elution peaks are plotted on the left-hand axes. Calculated molecular weights of monomers and dimers are shown with dotted red lines. (D) Kinetic analysis of the basal rate of GTP hydrolysis by *C. thermophilum* Vps1 GG. Initial rates of GTP hydrolysis at 37°C were plotted against the GTP concentration. The fit to the curve yielded k_{cat} and K_M . Each point is shown as mean \pm SD ($n = 3$).

Furthermore, we determined the structure of a similar Vps1 GG construct in complex with GDP (hereafter GG_{GDP}; Figs. 4 C and S4 A). GG_{GDP} crystallized with a single molecule in the asymmetric unit. A crystallographic twofold axis generated the same GTPase dimer around the nucleotide binding sites with a buried interface of 2,637 Å² (Fig. 4 G). The bound GDP was contacted by Lys56 in the P loop, which formed a hydrogen bond with the β -phosphate and the main chain amide nitrogens of Ser53, Ser54, Gly55, K56, and Ser57 (Fig. 4, H and I). Switches 1 and 2 were unusually well ordered for a GDP-bound GTPase structure due to stabilization by the dimer interface. Switch 1, however, was pulled away from the active site, which allowed several waters to enter. The BSEs in this structure were disordered (Fig. 4 G), perhaps due to steric clashing imposed by the crystal symmetry or due to the construct used. Refined density for each nucleotide is shown (Fig. 4 J).

GG_{GDP} showed overall deviations of C α s of 1.73 Å and 1.93 Å with GG_{GMPPCP} and GG_{GDP·AlF₄-}, respectively. Structural superpositions revealed several nucleotide-dependent conformational changes within the GTPase domain (Fig. 5). First, there was a significant

shift in Switch 1 with a maximum movement at Gln73 of 7.3 Å compared with GG_{GMPPCP} (Fig. 5 A) and 8.2 Å with respect to GG_{GDP·AlF₄-} (Fig. 5 B). These Switch 1 movements resulted in a shift of \sim 2.8 Å at the base of α 1 within the core GTPase fold (see Fig. S5 for a sequence alignment that details the nomenclature for the structural elements within GG). This movement was transmitted to and amplified at the loop between β 2B and β 3 at the base of the core β -sheets of the GTPase fold: His162 moved 7.4 Å compared with the GG_{GMPPCP} and 6.8 Å compared with the GG_{GDP·AlF₄-}. The shift in this loop resulted in movements at the bases of all the sheets in this region. β 2A and α B were pulled toward the repositioned β 2B (Fig. 5 C). These movements together resulted in a shift in the position of the loop between β 2A and α B (the α B loop; 3.1 Å). Interestingly, this lies adjacent to Insert A, most of which we observed in our GG_{GMPPCP} and GG_{GDP} structures. A morph of the movements of the Cas present in both GG_{GMPPCP} and GG_{GDP} is shown in Video 5. This movement also destroys an alignment of four hydrophobic residues observed in GG_{GMPPCP}- and GG_{GDP·AlF₄-} bound structures: Tyr126 (in β 2A- α B loop), Trp114 (in β 2A), Tyr159 (in β 2B), and Ile86 (in β 2; Fig. 5 D). Together, these resi-

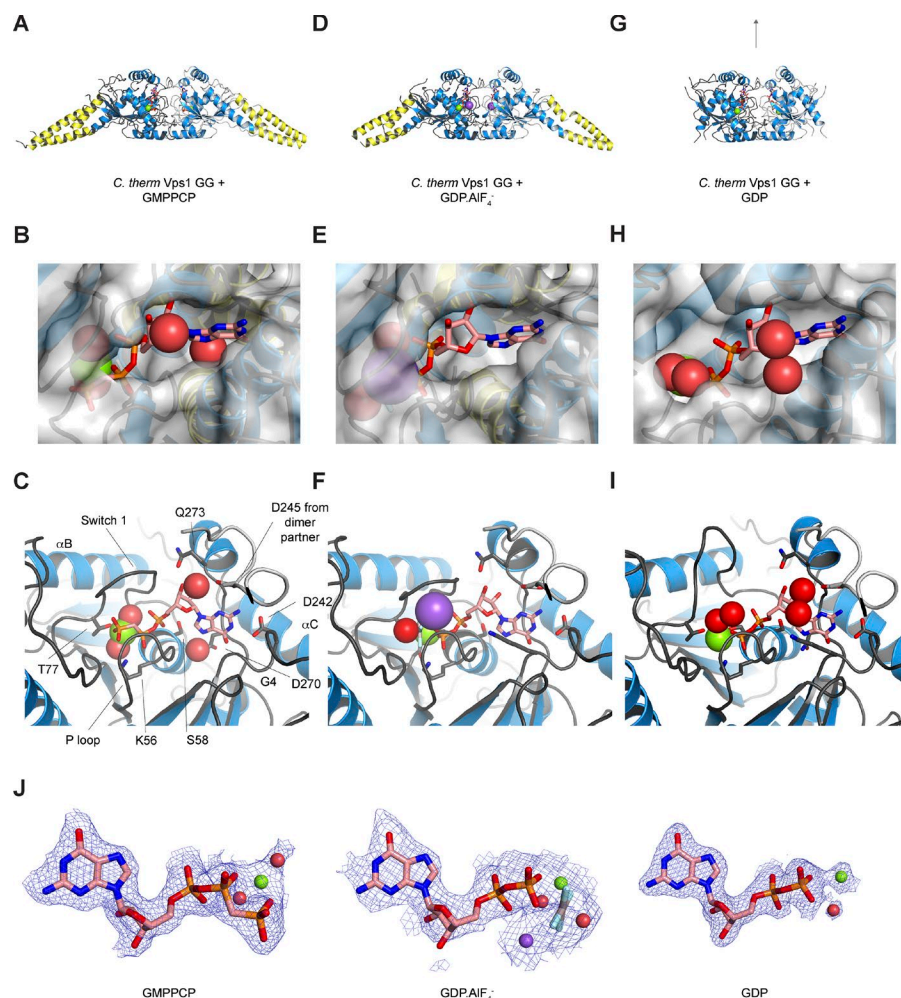


Figure 4. The crystal structures of *C. thermophilum* Vps1 GG in complex with GMPPCP, GDP·AlF₄⁻, and GDP. (A–C) The structure of Vps1 GG_{GMPPCP}. GMPPCP is shown in stick representation, and the Mg²⁺ is shown in green. Ordered waters are shown in red. **(D–F)** The structure of Vps1 GG_{GDP·AlF₄⁻}. GDP and AlF₄⁻ are shown as stick representations. Mg²⁺ and Na⁺ are shown as green and purple spheres, respectively. **(G–I)** The structure of Vps1 GG_{GDP}. A crystallographic twofold axis is shown as a gray arrow. No ordered density for BSE was observed. Coloring as in A. **(B, E, and H)** Nucleotide binding pockets for Vps1 GG_{GMPPCP}, GG_{GDP·AlF₄⁻}, and GG_{GDP} shown in A, D, and G with the molecular surface overlaid and shown transparently in gray. **(C, F, and I)** Details of the nucleotide-binding pockets of the structures shown in A, D, and G. **(J)** 2F_{obs} - F_{calc} maps (contoured at 1 σ) of the nucleotide, nucleotide analogue, or transition state analog of each structure.

dues form a “hydrophobic ridge.” When GG_{GMPPCP} and GG_{GDP·AlF₄⁻} were compared, small additional rotations in the Switch 1 region and the P loop were observed, which may have fine-tuned the conformation of the catalytic site for hydrolysis (Video 6).

Vps1 GG_{GMPPCP} crystallized with the BSEs in the open conformation, as did dynamin 1 GG bound to GMPPCP (Chappie et al., 2011). Comparison of the structures (Fig. S6 A) demonstrated that while the GTPase cores superpose well (overall core r.m.s. deviation, 1.17 Å), differences concentrate within the BSEs. In Vps1 GG_{GMPPCP}, the BSEs were rotated further away from the GTPase core than the BSEs in the dynamin-GMPPCP structure, resulting in a further opening out of the BSEs. The largest rotation was observed for the C_{GED} helix, where the helix rotated out a further 22.1° compared with the dynamin structure (Fig. S6 B). The N_{GTPase} helix rotated an additional 20.5°, while the C_{GTPase} helix rotated 16.9°. The result of this opening out was that the distance between comparable residues at the base of C_{GED} was 137.2 Å in Vps1 GG and 126.6 Å in the dynamin structure.

When compared with Vps1 GG_{GDP}, both Vps1 GG_{GMPPCP} and Vps1 GG_{GDP·AlF₄⁻} underwent a Switch 1 movement that was transmitted to the bases of the β-sheets, the β2A-αB loop, and the αB helix. Dynamin GG_{GMPPCP} behaved analogously to Vps1 GG_{GMPPCP} and underwent a comparable Switch 1 movement (Fig. S6 C; Chappie et al., 2011; Anand et al., 2016). The conformation of dynamin 1

GG_{GDP·AlF₄⁻}, however, was similar to that of dynamin 1 GG_{GDP} (Fig. S6 D; Chappie et al., 2010). This is because this GDP·AlF₄⁻-bound structure crystallized with the BSEs in the closed conformation rather than the extended and open conformation we observed for Vps1 GG_{GDP·AlF₄⁻}. The open BSE conformation was previously observed only with a GG construct for *Arabidopsis thaliana* DRP1A bound to GDP·AlF₄⁻ (Yan et al., 2011).

The cryoEM structure of full-length Vps1

To obtain mechanistic insight into self-assembly of Vps1, we characterized full-length Vps1 fused to MBP using EM. In the nucleotide-free state, Vps1 was heterogeneous and formed curved filaments (Fig. 6 A). Addition of GDP resulted in formation of rings with outer diameter 41.2 ± 1.9 nm (mean ± SD) and luminal diameter 17.2 ± 1.6 nm. When viewed side-on, we observed short stacks of rings or short helices (Fig. 6 A). Addition of GDP·AlF₄⁻ also yielded rings and short stacks (outer diameter 43.6 ± 3.5 nm; luminal diameter 20.9 ± 2.9 nm). By contrast, incubation with GMPPCP produced extended helices of uniform diameter of 39.3 ± 2.2 nm (Fig. 6 A). The GMPPCP-bound Vps1 tubes exhibited structural flexibility, which may represent an inherent ability of Vps1 to accommodate a range of templates of varying geometry. Nevertheless, these tubes were suitable for structural characterization by cryoEM (Fig. S7 A).

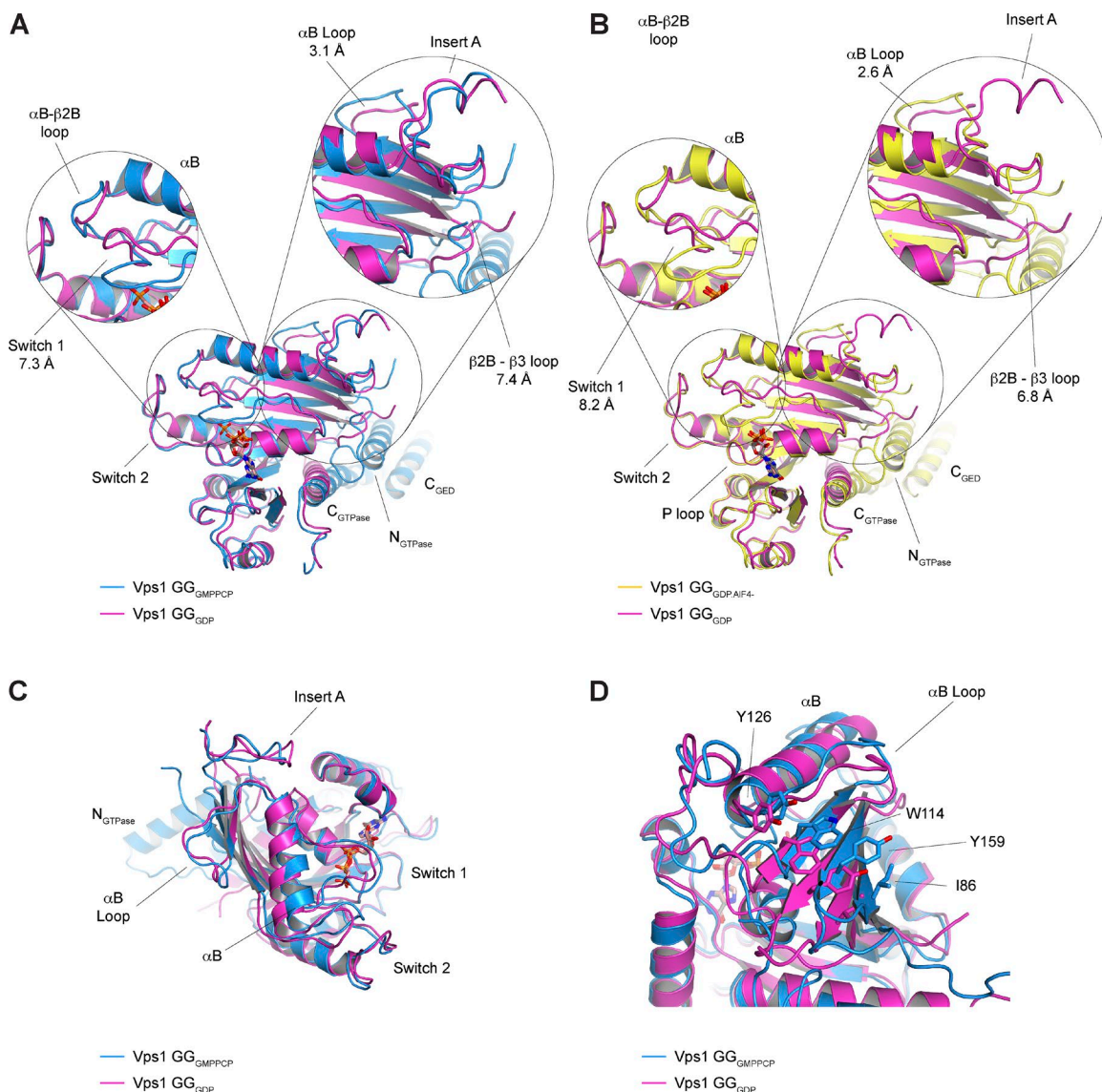


Figure 5. Nucleotide-dependent conformational changes in the Vps1 GG structures. (A) Superposition of Vps1 GG_{GMPPCP} (pale blue) and GG_{GDP} (pink). For ease of visualization, residues 270–299 have been omitted from both structures. (B) Superposition of GG_{GDP:AlF₄-} (gold) and GG_{GDP} (pink). As in A, residues 270–299 have been omitted. (C) An alternative view of the superposition shown in A. (D) Detail of the conformational shifts at the bases of the sheets of the core GTPase fold that bring Y126, W114, Y159, and I86 into alignment in GG_{GMPPCP} (blue) to create a hydrophobic ridge.

We determined the structure of the full-length Vps1 helical assembly assembled in the presence of GMPPCP to a global resolution of 11 Å using cryoEM and helical reconstruction (Fig. S7, A and B; He and Scheres, 2017). The helical tube had a luminal diameter of 19.1 nm and an outer diameter of 42.4 nm (Fig. S7 C). The tube was right-handed, 1-start, and had 14.9 subunits per turn with a pitch of 157 Å. The different domains of Vps1 are readily distinguishable in the density map (Fig. 6 B). Removal of the MBP tag after assembly by incubation with PreScission protease did not affect the helical assemblies (Fig. S7 D).

Comparison of our helical reconstruction of Vps1 with that of GMPPCP-bound dynamin 1 ΔPRD assembled on DOPS (Chappie et al., 2011) revealed several striking differences (Fig. 6, C–H). First, the Vps1 helix had an increased pitch (157 Å) compared with that of dynamin1 ΔPRD (99 Å; Fig. 6, C and D). This was due primarily to the increased tilt of the BSEs themselves in

the Vps1 helix (−37° to a plane perpendicular to the helical axis compared with 7° for dynamin 1 ΔPRD; Fig. 6, E and F). This generated the longer “arms” seen in the T view (Fig. 6, C and D). Second, the Vps1 helix had an increased tilt of the stalks and GTPases relative to a plane perpendicular to the helical axis in the Vps1 assembly (14.5° for Vps1 compared with 7.5° for dynamin 1 ΔPRD; Fig. 6, E and F). The Vps1 helical assembly had a more “open” architecture than dynamin 1 ΔPRD as a consequence of these differences. The Vps1 helix consisted of 14.9 subunits per turn with an outer diameter of 424 Å compared with 13.2 subunits per turn and 400 Å for dynamin 1 ΔPRD (Fig. 6, G and H). No density was visible for the region that would be occupied by Insert B, within the lumen of the helix, likely due to the conformational flexibility of the low-complexity sequence that comprises Insert B, whereas the positions of the PH domains adjacent to the lipid were clear in the case of the dynamin 1

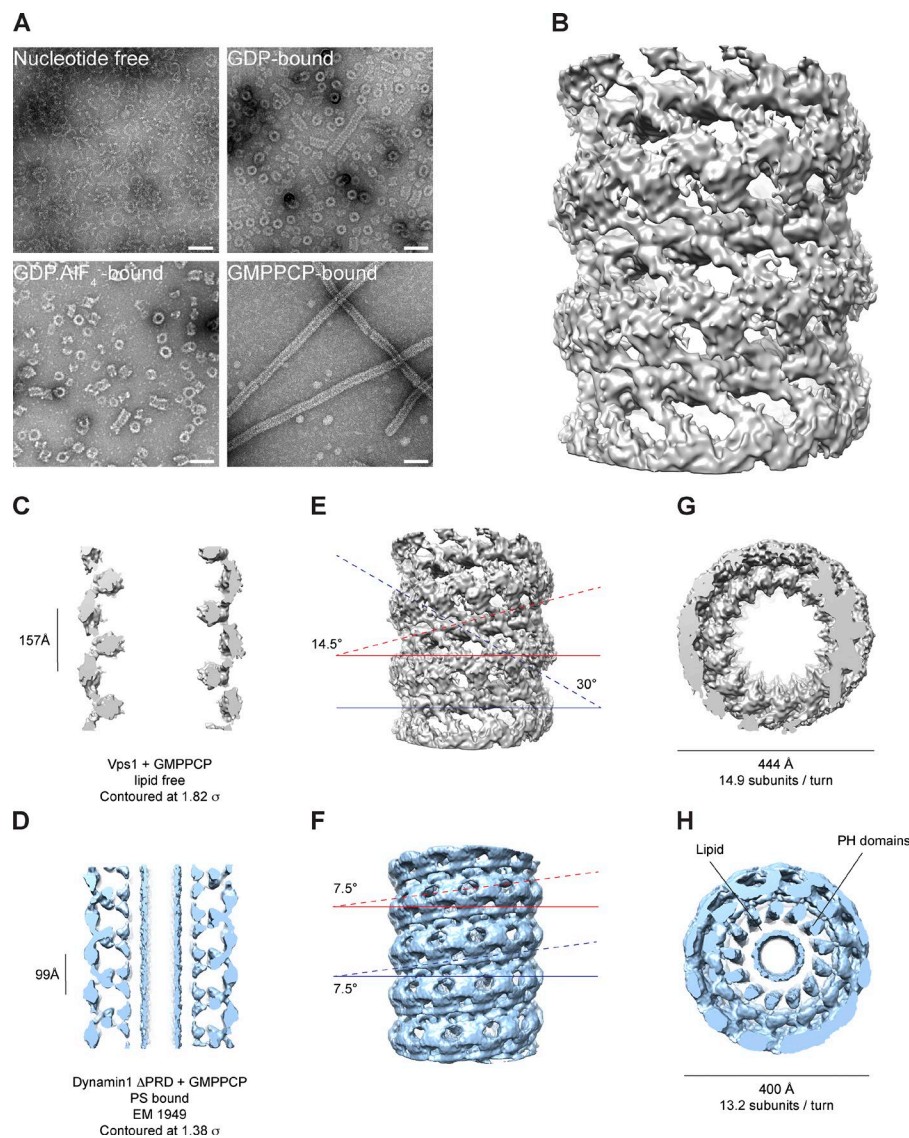


Figure 6. CryoEM reconstruction of the *C. thermophilum* Vps1 helical assembly bound to GMPPCP and comparison with dynamin 1 Δ PRD bound to GMPPCP and PS. (A) Effects of nucleotide binding on assembly of purified Vps1. EM projection images of negatively stained Vps1. Bars, 100 nm. **(B)** CryoEM density map of Vps1 bound to GMPPCP at 10.97 Å resolution and shown at a contour level of 1.82 σ . **(C and D)** Comparison of cross sections through the Vps1 (gray) and dynamin 1 Δ PRD (blue; contoured at 1.38 σ) assemblies. Slices parallel to the helical axis at the widest point of the helix were taken. **(E and F)** Comparison of the helical parameters of Vps1 and dynamin 1 Δ PRD. The angles subtended by the pairs of red and blue lines illustrate the angles of the GTPases and BSEs to a plane perpendicular to the helical axis, respectively. **(G and H)** End-on views of the Vps1 and dynamin 1 Δ PRD helices.

assembly (Fig. 6 H). In addition, no density was visible for the C-terminal MBP tag.

In contrast with dynamin, the BSE density in Vps1 made no contacts or interfaces with the densities for either Stalks or neighboring GTPase domains. The GTPase dimerization interface was readily discernible as expected for a GMPPCP-bound structure. We also identified a new second interface between adjacent GTPase domains (Fig. S7 E), which appeared to stabilize the open helical configuration of the Vps1 assembly.

A pseudoatomic model for Vps1

To understand the observed structural differences in our Vps1 reconstruction more fully, we generated a pseudoatomic model for the full-length Vps1 helix. Crystal structures of the Vps1 GG_{GMPPCP} dimer and the Stalk dimer from rat dynamin 1 Δ PRD (Ford et al., 2011) were sequentially docked as independent rigid units into the helical reconstruction (Fig. 7 A). Overall identity and similarity between *C. thermophilum* Vps1 and rat dynamin 1 across the stalk were 34% and 55%, respectively. Vps1 GG_{GMPPCP} fit well into the globular, bilobal density on the outer surface of the helix, with the

BSEs being placed into the thin rods of density connecting the GTPases to the stalks. The Stalk dimer easily fit into the Stalk density. The full helix was generated by applying the helical parameters to the positioned dimers, followed by a local optimization. The fit did not generate any steric clashes and required no additional manipulation to the atomic models (Fig. 7 B–G). Small gaps present between the tops of the Stalks and the ends of the BSEs could readily be accounted for by the residues missing in the docked models: seven amino acids between the end of the C_{GTPase} helix and the start of the Stalk and 10 amino acids between the end of the Stalk and the C_{GED} helix. Small protrusions of unfilled density remained at the bases of the stalks and were likely the start and end of the disordered Insert B sequence (Fig. 7 D). An additional small patch of unfilled density adjacent to the C_{GED} helix likely arose from the linker connecting Vps1 and MBP (Fig. 7 F).

Within the Stalk, Interface 3 at the bases of the stalks (facing the helix lumen) were formed as predicted from the linear filaments observed in the dynamin 1 Δ PRD and MxA crystals (Gao et al., 2010, 2011; Faelber et al., 2011; Ford et al., 2011) and in models of helical assemblies generated on the bases of these structures.

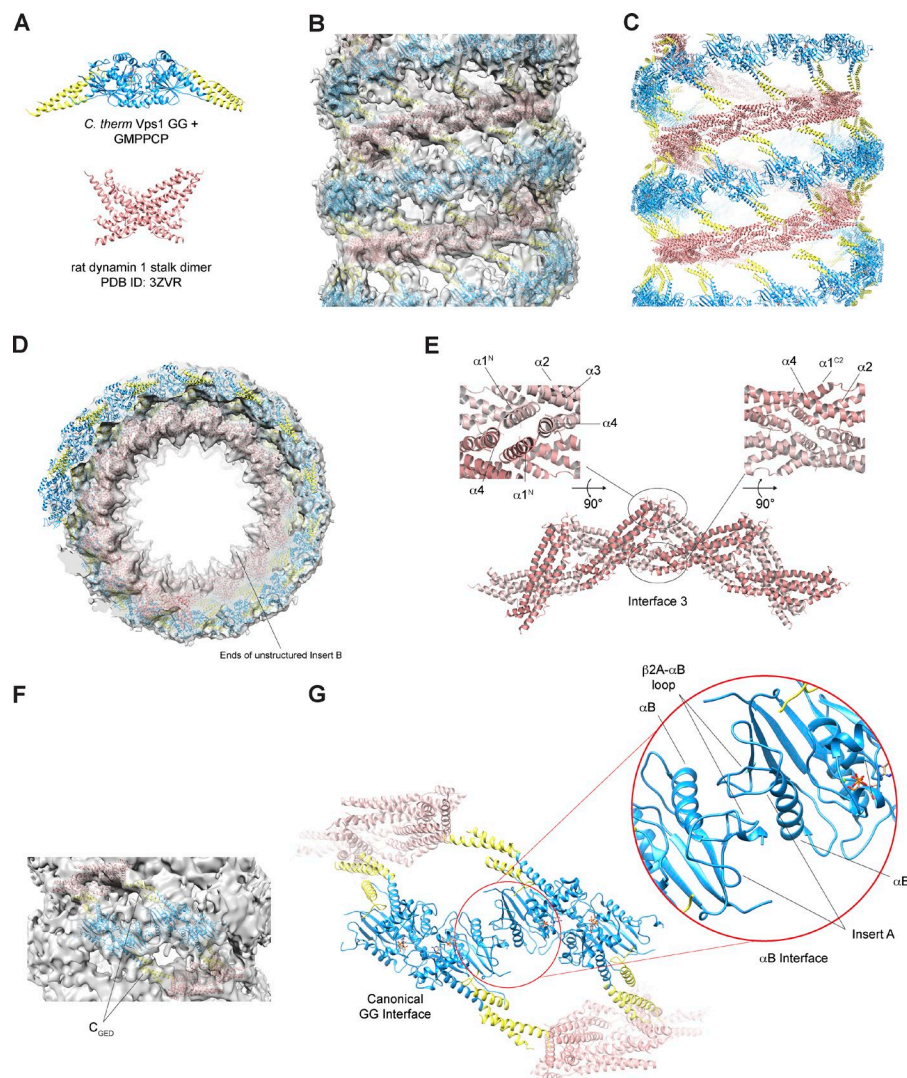


Figure 7. A pseudoatomic model of the *C. thermophilum* Vps1 assembly. (A) The building blocks used to assemble the pseudoatomic model: the Vps1 GG_{GMPPCP} dimer and the stalk domain dimer from rat dynamin 1 Δ PRD. (B) Assembled pseudoatomic structure generated by sequential docking and application of the refined helical parameters for the Vps1 GG_{GMPPCP} dimer and the stalk dimer. The fit of each of the positioned dimers was subsequently locally refined. (C) As for B but shown without the density from the reconstruction. (D) End-on view of the pseudoatomic model overlaid with the density. The protrusion of unfilled density facing the lumen of the helix, likely occupied by the start and end of Insert B, is indicated. (E) Assembly Interfaces 1 and 3 form between adjacent dimers at the stalk region (inner density layer). Four stalk dimers are shown. (F and G) Detail of the Vps1 assembly interfaces. (F) The fit of the pseudoatomic model showing two adjacent dimers within the Vps1 helical assembly, showing the canonical GG GTPase interface and the novel α B interface between neighboring GTPase domains. The C_{GED} helix, which directly connects to the linker at its C terminus, is labeled. (G) The α B interface, circled in red, is formed by the α B and the β 2A- α B loops from related GTPases.

This positioned the tight L2 loop between helices $\alpha 1^{C2}$ and $\alpha 2$ in the stalk, where the assembly-deficient mutations G436D (Vps1) and G397D (rat dynamin 1) are found, which is presumably the molecular basis for the assembly deficiency (Fig. S2, B and C). Furthermore, the “sticky patch,” which forms Interface 1 (Ford et al., 2011) between adjacent Stalk dimers, was again formed (Fig. 7 E). The fit also reinforced the observation from the density that the BSEs do not form any additional contacts with either the Stalks or adjacent GTPase domains, which is in contrast with what has been observed in dynamin crystal structures and in a model for the helical assembly (Chappie et al., 2011; Faelber et al., 2011; Reubold et al., 2015).

As predicted by the model, mutation of residues in either *C. thermophilum* Vps1 Interface 1 or Interface 2 disrupted Vps1 function as determined using both growth assays and by assessing vacuolar morphology (Fig. S8, A and B). By contrast, mutation of a residue not known to be involved in either Stalk interface or any other interactions (*C. thermophilum* Vps1 K498E) behaved as did WT *C. thermophilum* Vps1 when assessed using either assay.

We observed a novel interface formed by GTPases from adjacent rungs on the helix (Fig. 7 G). This interface was formed by close approach of the β 2A- α B loops (the α B loops) and Insert A from adjacent GTPase domains. The α B loop underwent sig-

nificant nucleotide-dependent conformational changes as observed in our crystal structures (Fig. 5 A), and hence formation of this interface may be context dependent. The close approach of adjacent Insert A in this interface may also be important for the formation or stability of this interface. Comparison of the residues that comprise the α B loops from several different DRP family members (Fig. S5) as well as variations in Insert A sequence demonstrates several differences in the solvent-facing residues that could contribute an additional layer of regulation on helix formation. We term this interface the α B interface.

Disruption of the α B interface abrogates Vps1 function in vivo

We mutated the α B loop and the surface-facing residues on the α B helix as a control in both *C. thermophilum* Vps1 and *S. cerevisiae* Vps1. Expression of *C. thermophilum* or *S. cerevisiae* Vps1 bearing a mutated α B loop did not rescue growth of Δ vps1 cells at 37°C nor rescue the defect in vacuolar morphology (Fig. 8, A–D). By contrast, mutation of the surface-facing residues on the α B helix, which are not predicted to be involved in the formation of this interface, behaved like WT Vps1. Furthermore, while *S. cerevisiae* Vps1-EGFP rescued CPY maturation in Δ vps1 cells, Vps1 bearing a mutated α B loop did not (Fig. S8 C).

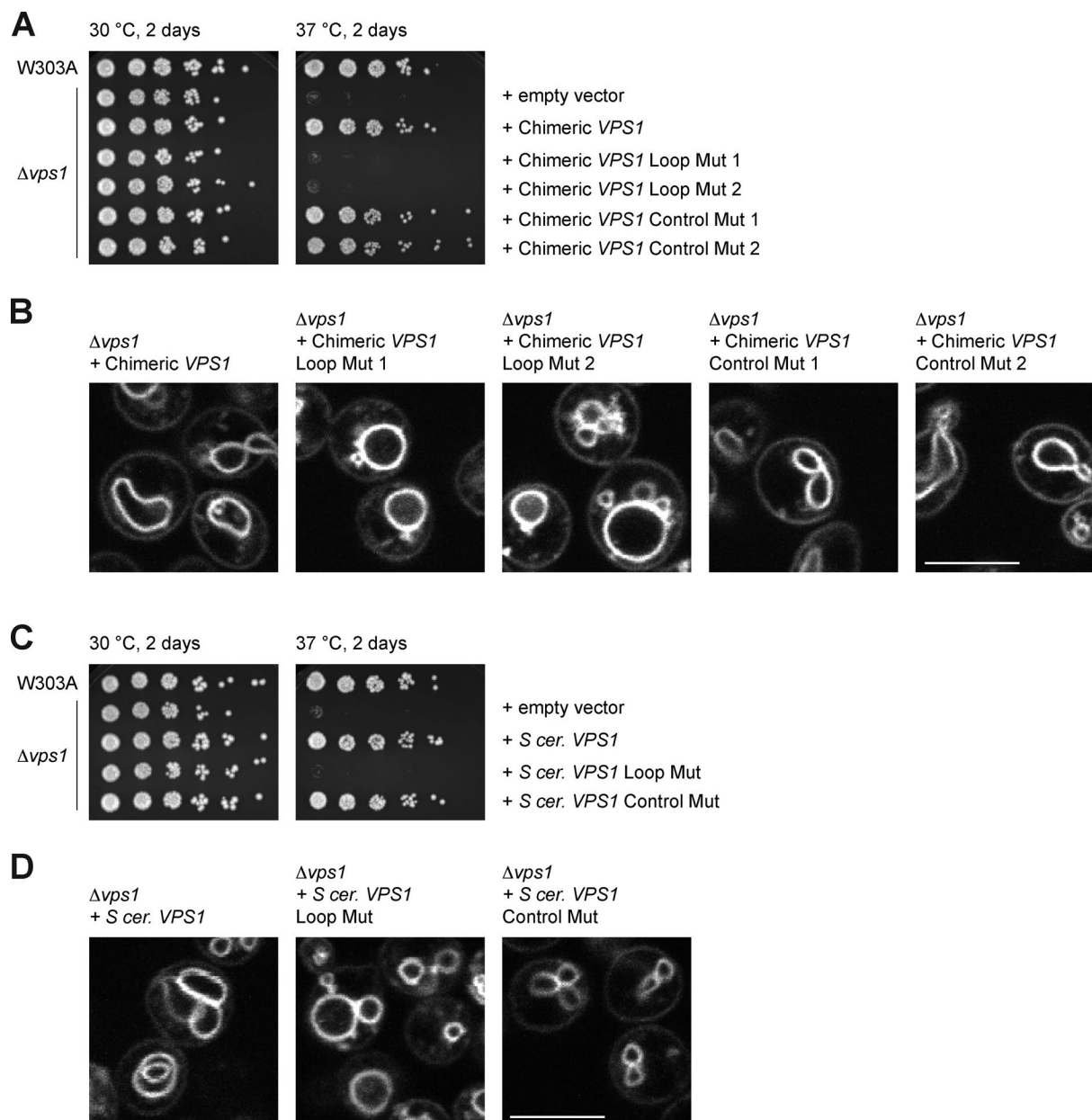


Figure 8. **Disruption of the α B loop interface abrogates Vps1 function in vivo.** (A) Plasmids containing *C. thermophilum* Vps1 harboring mutations in either the α B loop (Loop Mut 1 and 2) or in the α B helix (Control Mut 1 and 2) were expressed in $\Delta vps1$ cells. Growth was assessed on YPD plates at 30 or 37°C after 2 d. (B) Vacuolar morphology was assessed in $\Delta vps1$ cells expressing the loop and control mutants as in A. Vacuoles were visualized using FM 4–64. (C and D) As in A and B but using corresponding mutants in *S. cerevisiae* Vps1. Bars, 5 μ m.

Discussion

DRPs are mechanochemical enzymes that are responsible for numerous membrane-remodeling events within the cell. How the general fundamental features of DRP function are adapted to specific cellular targets and functions is an area of outstanding interest. In this study, we extensively characterized the fungal DRP Vps1. Vps1 preferentially assembles at the endosomal compartment and regulates its function. We present crystal structures of minimal Vps1 GG constructs in different nucleotide states that capture several steps of the catalytic pathway and reveal unique features on the GTPase domain that are determinants of a novel biologically important interface that forms during Vps1 helical

self-assembly. We show by cryoEM that assembled full-length Vps1 has a looser packing when compared with the helix formed by dynamin 1 that may provide it with appropriate flexibility to accommodate its preferred cellular template. Pseudoatomic modeling that combined our crystallographic and EM structures identified a novel, biologically important interface that forms during Vps1 helical self-assembly.

Our data show that Vps1 self-assembly is required for its function at the endosomal compartment. Vps1 G436D, the equivalent of the assembly-defective dynamin mutation G397D, cannot rescue endosomal function, as assessed using several assays. Conversely, expression of Vps1 K42A, the equivalent of dynamin

K44A, which can be trapped in a hyperconstricted prefission state, results in formation of few large assemblies within the cell that are invariably associated with the endosomal compartment. Although Vps1 has been reported to act at several sites within the cell, trapped Vps1 assemblies are always localized to the endosomal compartment. Hence, the primary site of action of Vps1 is the endosomal compartment. It is possible that Vps1 can be recruited to and assemble at other sites within the cell but that the K42A mutation, for unknown reasons, preferentially becomes trapped at the endosome.

The helical reconstruction of the GMPPCP-bound Vps1 assembly revealed a more open and looser helix than that observed for GMPPCP-bound dynamin 1. Structural comparison showed significant differences in the orientation of the BSEs in the assembled helices. These changes resulted in the increased pitch of the Vps1 helix and the concomitant additional space between adjacent rungs. The BSEs in Vps1 also did not appear to engage in any interfaces, unlike in models for helically assembled dynamin and in the linear dynamin filaments captured in the crystal structures. Strikingly, Drp1 assembled on nanotubes exhibits a pitch of ~130 nm, approximately intermediate between what is observed for dynamin and Vps1 (Francy et al., 2017). Since Vps1, dynamin 1, and Drp1 all exhibit different pitches and overall architectures and are known to function at different cellular targets, it is of course tempting to speculate that the helical architectures of DRPs have been extensively customized for their appropriate cellular targets.

Vps1 GTPase domains interact across the rungs of the helical assembly at two distinct interfaces. The first is the canonical head-to-head dimerization interface that has been observed in all DRP assemblies and brings the active sites together for reciprocal stimulation of catalytic turnover. The second, which we term the α B interface, arises from the close approach of the α B loops and Insert A in neighboring subunits. The likely function of this interface is to further stabilize the open architecture of the Vps1 assembly. Disruption of this interface abrogated Vps1 function in vivo. Our GG crystal structures showed that this region exhibits significant nucleotide-dependent conformational changes. The function of Insert A remains unknown. It is present in all DRPs with the exception of dynamin. It is not conserved among Vps1 family members and ranges in length from 27 residues in *C. thermophilum* Vps1 to 47 residues in *S. cerevisiae* Vps1. However, our pseudoatomic model revealed close approach of Insert A from adjacent GTPase domains in the α B interface. We therefore speculate that Insert A may be required to form or stabilize this interface.

One striking difference between Vps1 and dynamin 1 is the robust stimulation of dynamin GTPase activity observed in the presence of liposomes, whereas stimulation of Vps1 by liposomes is minimal. Several possibilities may account for this difference. First, dynamin self-assembles into helical polymers with or without lipid substrate regardless of nucleotide triphosphate load, but its GTPase activity is only stimulated in the presence of negatively charged phospholipids. The dynamin PH domain is critical for regulation and facilitation of lipid-stimulated GTP hydrolysis. We only observed helical assembly of Vps1 on pre-formed nanotubes and not on liposomes similar to those that

have typically been used to stimulate dynamin GTPase activity. Instead of a PH domain, Vps1 has Insert B. Insert B may have a differing lipid preference when compared with the PH domain or may be a site for posttranslational modifications, regulating targeting to or avidity for lipids. Second, different patterns of BSE or noncanonical GTPase–GTPase interactions in assembled Vps1 compared with dynamin may result in the observed differences between Vps1 and dynamin. Indeed, the architecture of assembled Vps1 lacks additional contacts between the extended BSEs and neighboring Stalks/GTPases, whereas models of assembled dynamin do predict additional contacts. These may contribute to formation of a hydrolysis-competent conformation of GTPase domains of assembled dynamin.

Vps1 can assemble on lipid nanotubes containing PI3P. One avenue for future enquiry is to determine the lipid-bound structure of Vps1 and to determine how lipid binding affects the general architecture of Vps1 helical assemblies. Although our current structure is full-length, Insert B is disordered. Since Insert B would be lipid facing in a lipid-bound helix, its function is likely to mediate lipid interaction either directly or indirectly. In addition, we observed that deletion of Insert B prevented self-assembly even in the absence of lipids (unpublished data). In cells, Vps1 Δ InsB had a diffuse cytosolic distribution, and purified Vps1 Δ InsB could not assemble even in the absence of lipids. Therefore, Insert B is likely required both for lipid interaction and for Vps1 helical assembly.

Collectively, our study provides insight into the mechanistic determinants in Vps1 that tailor it for the generation of open and flexible helices, which are likely to be required for its endosomal functions. Various DRPs like Dnm1 and Drp1 more closely resemble Vps1 than dynamin in that they have an Insert A and B and lack PH and PRD domains. This study therefore has important implications for defining the mechanistic and structural relationships among dynamin family members and underscores the fundamental principles of helix assembly in these proteins.

Materials and methods

Yeast genetic manipulation and molecular biology

Strains of *S. cerevisiae* used in this study are listed in Table S1. Gene deletions were generated in W303A/ α diploids by homologous recombination using appropriate cassettes amplified from pFA6a-kanMX6, pFA6a-His3MX6, or pFA6-natMX4 (Longtine et al., 1998; Goldstein and McCusker, 1999) flanked with a sequence (30 nt) proximal to the coding sequence of the target gene. Diploids were subsequently sporulated by starvation in SPO (1% potassium acetate, 0.1% yeast extract, and 0.05% glucose) medium for 2 d. Following manual tetrad dissection, knockout haploids were extensively validated. Deletion strains were generated at 30°C with the exception of Δ vps1::NAT, where all construction stages from sporulation onwards were conducted at room temperature.

Yeast media

YPD (2% yeast extract, 1% peptone, and 2% glucose supplemented with L-tryptophan and adenine) was used for routine growth. Synthetic complete (yeast nitrogen base, ammonium sulfate, 2% glucose, and amino acids) or synthetic defined (yeast nitrogen

base, ammonium sulfate, 2% glucose, and appropriate amino acid dropout) media were used before microscopy or to maintain plasmid selection as required. Cells were induced to sporulate by overnight incubation in YPA (2% potassium acetate, 2% peptone, and 1% yeast extract) followed by incubation in SPO.

Cloning

Select plasmids used in the course of this study are detailed in Table S2. *S. cerevisiae* *VPS1* was amplified from W303A/ α genomic DNA, prepared using the Yeast DNA Extraction kit (Thermo Fisher Scientific). *C. thermophilum* *VPS1* was amplified from *C. thermophilum* cDNA (Amlacher et al., 2011). All constructs were generated by splicing by overlap extension and Gibson assembly. *C. thermophilum* *VPS1* was fused at its C terminus to MBP and cloned into pcDNA3.1⁺ for expression in mammalian cells. The following GG constructs were used: pET-15b PreScission-*C. thermophilum* *VPS1* GG, where residues 355–668 of the *VPS1* coding sequence were replaced with an AGAGA linker and pET-15b *C. thermophilum* *VPS1* G-EGFP-G, where residues 359–668 of the *VPS1* coding sequence were replaced with a cassette consisting of an AG–PreScission site–EGFP–PreScission site–GA construct.

Analysis of growth by serial dilution

Following overnight growth in appropriate media, cells were diluted and regrown to mid-logarithmic phase in YPD at 30°C (OD₆₀₀ 0.6–0.8). Cells were then diluted to 0.5 OD₆₀₀/ml, and fivefold serial dilutions were made in water. 2 μ l of each dilution was spotted onto YPD plates, after which the cells were incubated at 30 or 37°C for 2 or 3 d before imaging.

Western blotting

Protein extracts for Western blotting were obtained as described previously (Millen et al., 2009). In brief, cells were lysed on ice by resuspension in 1 ml ice-cold H₂O supplemented with 150 μ l 1.85 M NaOH and 7.5% (vol/vol) β -mercaptoethanol. Protein was precipitated by addition of 150 μ l 50% (wt/vol) TCA. Pellets were washed twice with acetone, resuspended in 150 μ l 1 \times SDS-PAGE buffer, and incubated for 30 min at 30°C followed by 2 min at 95°C. Antibodies used were as follows: anti-PGK1 (ab113687; Abcam), anti-CPY (ab34636; Abcam), and anti-EGFP (ab290; Abcam). Labeled secondary antibodies were IRDye 680RD goat anti-rabbit antibody (926-68171; LI-COR Biosciences) and IRDye 680RD goat anti-mouse (926-68070; LI-COR Biosciences). These were detected using the Odyssey system (LI-COR Biosciences). Bands were integrated and quantified using the Fiji distribution of ImageJ (National Institutes of Health; Schindelin et al., 2012).

Preparation of yeast for microscopy

Cells were grown overnight in YPD or synthetic defined medium appropriately supplemented to maintain plasmid selection. Cells were then diluted in YPD and grown to mid-logarithmic phase. Vacuolar membranes were stained with 10 μ M FM 4–64 (Thermo Fisher Scientific) for 45 min followed by washing and incubation in YPD medium without dye for 1 h. Cells were plated onto No. 1.5 glass-bottomed cover dishes (MatTek Corporation) previously treated with 15 μ l of 2 mg/ml concanavalin A (Sigma-Aldrich).

Confocal microscopy and image analysis

Confocal images were acquired on a Nikon A1 confocal microscope with a Plan Apochromat 100 \times oil objective. NIS Elements Imaging software (Nikon) was used to control acquisition. Images were further processed using Fiji or NIS Elements.

Sequence alignment

Sequence alignments were generated using MUSCLE (Edgar, 2004) and were formatted for presentation using the output produced by ESPript 3.0 (Robert and Gouet, 2014).

Protein expression and purification

Full-length *C. thermophilum* Vps1 was expressed in mammalian cells using the Expi293 Expression System (Invitrogen). Cells were transfected with plasmid DNA encoding a *C. thermophilum* Vps1-MBP fusion construct following the recommended protocol. 48 h after transfection, cells were washed twice with ice-cold PBS, and the pellet was resuspended in HNG buffer (50 mM Hepes/KOH, pH 8, 500 mM NaCl, and 5% glycerol) supplemented with 5 mM MgCl₂, 10 mM β -mercaptoethanol, 1% Tween-20, 0.3% NP-40, 50 μ g/ml DNase I, and the Halt Protease Inhibitor Cocktail (Thermo Fisher Scientific). After incubation at 4°C for 1 h, the lysate was homogenized using a Dounce homogenizer. The resulting homogenate was centrifuged at 21,000 g for 30 min at 4°C. The supernatant was incubated with amylose agarose resin (New England Biolabs) for 1 h at 4°C. The beads were extensively washed with HNG, then with HNG supplemented with an additional 500 mM NaCl, and then HNG again. The protein was then eluted using HNG supplemented with 100 mM maltose and protease inhibitor cocktail. The protein was concentrated and flash frozen for long-term storage at –80°C until use.

C. thermophilum Vps1 GG and *C. thermophilum* Vps1 G-EGFP-G were expressed overnight at 21°C by IPTG induction in BL21 cells grown in 2 \times TY. Cells were pelleted, washed, and resuspended in TN buffer (20 mM Tris/Cl, pH 8.0, 150 mM NaCl, and 1.93 mM β -mercaptoethanol). After homogenization using an Emulsiflex-C3 (Avestin), lysates were clarified by centrifugation at 142,000 g for 45 min at 4°C. Clarified lysates were applied to Ni-IDA beads in batch (Macherey Nagel). The beads were extensively washed and loaded into a column, and then protein was eluted in TN with a gradient to 250 mM imidazole. Peak fractions were pooled and dialyzed against TN to remove imidazole. Both proteins were then digested with PreScission protease at room temperature: in the case of *C. thermophilum* Vps1 GG, to remove the N-terminal tags, and in the case of *C. thermophilum* Vps1 G-EGFP-G, to excise the EGFP. *C. thermophilum* Vps1 GG was further purified by anion exchange chromatography and SEC, equilibrated in 5–20 mM Hepes, pH 7.4, 150 mM NaCl, and 1.93 mM β -mercaptoethanol using a Superdex 200 16/60 column (GE Healthcare). Following cleavage, *C. thermophilum* Vps1 G-EGFP-G was rebound to Ni-IDA (to remove cleaved EGFP), eluted, and dialyzed. Purification was completed as for *C. thermophilum* Vps1 GG. Proteins were concentrated and flash frozen in liquid nitrogen until use. Rat dynamin 1 (with a PreScission site engineered at the start of the PRD) was expressed in BL21(DE3) pLysS (Promega) cells as an N-terminal His₆ fusion using the pET-15b vector. Protein expression was induced as for Vps1 GG. Cells

were resuspended in 20 mM Tris/Cl, pH 8.0, 500 mM NaCl, and 1.93 mM β -mercaptoethanol and then were lysed, clarified, and bound to Ni-IDA. Protein was subsequently dialyzed and passed over ion exchange and size exclusion as for Vps1 GG using Tris/Cl, pH 8.0, 500 mM NaCl, and 1.93 mM β -mercaptoethanol as a running buffer. The protein was then concentrated, supplemented with glycerol to 10%, and frozen for long-term storage.

Human dynamin 1 GG was expressed in *Escherichia coli* as an MBP fusion and purified as described previously (Chappie et al., 2009) via amylose affinity, anion exchange following removal of the tag by PreScission protease cleavage, and SEC. The protein was dialyzed into a final buffer of 20 mM Hepes, pH 7.5, 150 mM KCl, 4 mM MgCl_2 , 2 mM EGTA, and 1 mM DTT during the final SEC step on a Superdex 75 10/300 GL column. Peak SEC fractions were collected, concentrated to 100–200 μl , flash frozen in aliquots, and stored at -80°C .

Preparation of liposomes and nanotubes

Liposomes were made from 100% DOPS, and nanotubes were made from 40% D-galactosyl- β -1,1'-N-nervonoyl-D-erythro-sphingosine, 40% DOPS, and 20% PI3P (Avanti). Lipids in chloroform were mixed in a glass tube with methanol added to keep the solution clear in the case of nanotubes containing PI3P. The mixtures were dried using a stream of nitrogen gas and were desiccated for at least 30 min. Liposomes and nanotubes were rehydrated in 20 mM Hepes/NaOH, pH 7.4, and 150 mM NaCl to a lipid concentration of 0.5 mg/ml. DOPS liposomes were subsequently extruded through a 1- μm Nucleopore membrane (Whatman).

GTPase assays

Continuous GTPase assays using the GTP regenerating system were performed as previously described (Ingerman and Nunnari, 2005) with the exception that reaction mixes without GTP were preincubated at 37°C for 10 min before addition of GTP to a final concentration of 1 mM. Reactions contained 142.5 mM NaCl, 7.5 mM KCl, and 5 mM MgCl_2 and were conducted at pH 7.0.

The colorimetric GTPase assay used to determine the kinetic parameters for Vps1 GG was performed using the malachite green phosphatase assay kit (Echelon Biosciences). Reactions contained 142.5 mM NaCl, 7.5 mM KCl, and 5 mM MgCl_2 and were performed at pH 7.0. Reactions were preincubated at 37°C for 10 min before addition of GTP at various final concentrations. Samples were withdrawn at several time points, and reactions were stopped by addition of EDTA, pH 8.0, to a final concentration of 100 mM. Malachite green reagent was added in accordance with the manufacturer's guidelines, and absorbance was determined after 30 min at 630 nm. Amount of phosphate released was determined using a standard curve. Kinetic parameters were calculated numerically by fitting data to the Hill Equation using a nonlinear least squares method as implemented in Prism (GraphPad Software).

Analytical SEC

Vps1 GG or dynamin 1 GG (19 μM) were preincubated where indicated in the absence or presence of the relevant nucleotide or nucleotide analogue (2 mM) for 1 h at 37°C . Samples were then loaded onto a Superdex 75 10/300 column preequilibrated in a

running buffer of 20 mM Hepes, pH 7.4, 150 mM NaCl, 5 mM MgCl_2 , 2 mM EGTA, and 1.93 mM β -mercaptoethanol, and elution volumes were recorded and compared. Gel filtration standards (Bio-Rad) were run in the same buffer.

SEC-MALS

Purified *S. cerevisiae* Vps1 G436D (4.0 mg/ml) was subjected to SEC using a Superdex 200 10/300 GL equilibrated in SEC-MALS buffer (20 mM Hepes, pH 7.5, 150 mM NaCl, 5.0 mM MgCl_2 , 2.0 mM EGTA, and 2.0 mM β -mercaptoethanol). *C. thermophilum* Vps1 GG (2.5 mg/ml) and Vps1 GG K56A (4.0 mg/ml) were subjected to SEC using a Superdex 75 10/30 equilibrated in SEC-MALS buffer. Nucleotide-dependent oligomerization was assessed by incubating with various nucleotides at 2.0 mM for 1 h at 37°C followed by centrifugation at 13,000 g for 10 min before SEC-MALS analysis. The gel filtration column was coupled to a static 18-angle light-scattering detector (DAWN HELEOS-II) and a refractive index detector (Optilab T-rEX; Wyatt Technology). Data were collected continuously at a flow rate of 0.5 ml/min. Data analysis was performed using the program Astra VI. Monomeric BSA (6.0 mg/ml; Sigma-Aldrich) was used for normalization of the light-scattering detectors and data quality control.

Crystallization

Prior to crystallization, *C. thermophilum* Vps1 GG (73 μM) was preincubated with 1 mM β , γ -methyleneguanosine 5'-triphosphate (GMPPCP; Sigma-Aldrich) for 1 h at room temperature in 5 mM Hepes, pH 7.4, 150 mM NaCl, 5 mM MgCl_2 , and 1.93 mM β -mercaptoethanol. Crystals were obtained by hanging drop vapor diffusion at room temperature, by equilibration of droplets of 5–6 μl containing 18.25–36.5 μM protein and 0.5 mM GMPPCP against a reservoir of 400 μl containing 14% PEG 4000, 0.2 M sodium acetate, and 0.1 M Tris/Cl, pH 8.7–9.0. Crystals appeared after 24–48 h. Crystals were cryoprotected by sequential transfer through solutions of the crystallization condition supplemented with 0.5 mM GMPPCP and increasing concentrations of PEG 400 to a final concentration of 15%. *C. thermophilum* Vps1 GG bound to $\text{GDP}\cdot\text{AlF}_4^-$ was generated by incubating 25 or 50 μM protein in 5 mM Hepes, pH 7.4, 150 mM NaCl, 5 mM MgCl_2 , and 1.93 mM β -mercaptoethanol with 2 mM GDP, to which NaF was added sequentially with vortexing to a final concentration of 20 mM, and to which AlCl_3 was added to a final concentration of 2 mM. The sample was then passed through a cellulose filter of 0.22- μm pore size before setup. Crystals were grown by vapor diffusion using 5- μl droplets containing 12.5 or 25 μM protein and 1 mM $\text{GDP}\cdot\text{AlF}_4^-$ against a reservoir of 400 μl containing 5–10% PEG 8000, 20% glycerol, and 0.08 M MES, pH 5.6–6.2, at room temperature. Crystals appeared after 24 h. Crystals required no additional cryoprotection and were flash cooled in liquid nitrogen for storage. Crystals of *C. thermophilum* Vps1 GG bound to GDP were obtained by preincubation of protein with 2.3 mM GDP in 5 mM Hepes, pH 7.4, 150 mM NaCl, 5 mM MgCl_2 , and 1.93 mM β -mercaptoethanol. Crystals were grown by vapor diffusion at room temperature against a reservoir of 400 μl containing 14–19% PEG 4000, 0.07–0.1 M trisodium citrate, and 20% isopropanol using 5- μl droplets containing 12.5 or 25 μM protein with 1.15 mM GDP, and crystals ap-

peared after 24–48 h. Crystals were cryoprotected by transfer to a solution containing 18% PEG 4000, 0.07 M trisodium citrate, and 20% isopropanol, and then substitution of the solution took place with the same supplemented with increasing amounts of PEG 400 to a final concentration of 10%. Cryoprotected crystals were flash cooled in liquid nitrogen for storage.

Crystallographic data collection, structure determination, and refinement

Reflection data for *C. thermophilum* GG_{GMPPCP} crystals were collected at 100K at ID-22 at the Advanced Photon Source (Argonne National Laboratory, Lemont, IL) at a wavelength of 1 Å using an Eiger detector. Crystals were monoclinic and belonged to spacegroup P2₁ with cell axes $a = 83.03$, $b = 120.18$, $c = 85.04$ Å, and $\beta = 120.22^\circ$. A dataset was collected using a single crystal to minimum Bragg spacings of 2.26 Å. The Vps1 GG_{GDP.AIF4} crystals were also monoclinic (spacegroup P2₁) with cell dimensions $a = 69.04$, $b = 121.16$, $c = 104.73$ Å, and $\beta = 90.62^\circ$. Reflection data were collected to a resolution of 3.1 Å. GG_{GDP} crystals belonged to spacegroup R3₂ and had cell dimensions $a = b = 84.98$ and $c = 271.50$ Å. A complete dataset was collected to a resolution of 2.13 Å. Reflection data were indexed and integrated using iMOSFLM (Battye et al., 2011). All data were scaled using Aimless (Evans, 2006) from the CCP4 suite of crystallographic software (Collaborative Computational Project, Number 4, 1994). Data collection statistics are shown in Table S3.

The GG_{GMPPCP} structure was solved by molecular replacement using Phaser (McCoy et al., 2007) as implemented in Phenix (Adams et al., 2010). The structure of *Homo sapiens* dynamin 1 GG bound to GMPPCP (PDB ID 3ZYC; Chappie et al., 2011) was used as a search model. Two complete dimers were present in the asymmetric unit. GG_{GDP.AIF4} was solved using a chain A from 3ZYC as the search model. Four copies were placed, which together created the two dimers within the asymmetric unit. GG_{GDP} was solved using chain A from the structure of dynamin 1 GG bound to GDP.AIF₄[−] (PDB ID 2X2E; Chappie et al., 2010). The structure had a single molecule within the asymmetric unit.

All models were completed and improved by iterative rounds of refinement using phenix.refine (Afonine et al., 2012) and COOT (Emsley et al., 2010). The structures were refined using restrained coordinate and individual B factor refinement together with parameter refinement for translation/libration/screw (TLS) groups identified using the Phenix interface. Early rounds incorporated simulated annealing. Refinement statistics and final model geometries are shown in Tables S4 and S5. Densities for the C_{GED} helices of molecules D in both the GG_{GMPPCP} and GG_{GDP.AIF4} structures were weak. All images were made using Pymol 1.7.6.0 (Schrödinger, Inc.) and UCSF Chimera (Pettersen et al., 2004). Coordinates and structure factors for GG_{GMPPCP}, GG_{GDP.AIF4}, and GG_{GDP} have been deposited in the Protein Data Bank with PDB IDs 6DEF, 6DJQ, and 6DI7, respectively.

EM

Sample preparation

To induce formation of Vps1 assemblies, Vps1 was diluted into assembly buffer (20 mM MES, pH 5.5, 1 mM MgCl₂, and 2 mM

EGTA) to yield final NaCl and protein concentrations of ~150 mM and 0.5–1 mg/ml, respectively. Samples were incubated for the indicated periods of time.

Negative-stain EM

Sample aliquots (3 µl) were adsorbed to glow-discharged 400-mesh carbon-coated copper grids and stained with 2% uranyl formate. Images were recorded on a TF20 electron microscope (FEI) equipped with a field emission gun at the indicated magnification on a 4,000 × 4,000 Gatan Ultrascan charge-coupled device camera.

CryoEM

3 µl of 0.5 mg/ml tubes were applied on the carbon side of glow-discharged holey R2/1 Quantifoil grids (Quantifoil Micro Tools GmbH), manually blotted from the back side, and then plunge frozen in liquid ethane using a homemade manual plunger. Images were collected at the Electron Bio-Imaging Centre at Diamond Light Source under low-dose conditions (~40 e[−]/Å² total) using a Titan Krios 300-kV microscope equipped with a Schottky X field emission gun and a Gatan Quantum energy filter with K2 Summit detector. Videos (6,426; each with 40 frames) were collected using EPU software (FEI) at a nominal magnification of 98,000 (1.06 Å/pixel) with under focus values ranging from 1.5 to 3.5 µm.

Image processing and helical reconstruction

Video frames were aligned using UCSF MotionCor2 (Zheng et al., 2017), and the resulting aligned videos were used for contrast transfer function estimation using CTFFIND4 (Rohou and Grigorieff, 2015). Micrographs were subsequently used for helical reconstruction using RELION 2.0 (He and Scheres, 2017). Helical segments were boxed using EMAN 2.0 e2helixboxer.py (Tang et al., 2007), and Fourier transforms from individual tubes or 2D class averages generated using SPRING (Desfosses et al., 2014) were used to estimate the helical parameters. A small dataset with 953 segments (500-pixel box size) was used in iterative helical real space reconstruction (IHRSR; implemented in SPIDER; Egelman, 2007; Shaikh et al., 2008) to refine the helical parameters, which converged to a rotation angle of 24.07° and a 10.48 Å rise. The full dataset containing 29,692 segments (600-pixel box size [scaled to 400], 90.41% overlap between neighboring boxes, and inter-box distance 6× helical rise) was used in the helical processing workflow in RELION 2.0. The segments were analyzed by 2D classification, and classes showing clear structural details were selected for further processing (26,485 segments correspond with ~158,000 subunits). The first round of refinement, using a featureless cylinder (400 pixels in diameter; low pass filtered to 30 Å), resulted in a map with resolution of 16.7 Å. This was used as an initial reference for the subsequent rounds of refinement, which resulted in a final density map at 11 Å after B-factor sharpening and application of a soft-edged mask. Further 3D classification did not reveal distinguishable 3D classes. The final EM map has been deposited with the EM Databank with ID code 7874.

Online supplemental material

Fig. S1 shows characterization of endosomal trafficking in $\Delta vps1$ cells. Fig. S2 shows characterization of the Vps1 K42A and G436D mutants. Fig. S3 shows biochemical characterization of Vps1. Fig. S4 shows the structures of Vps1 GG bound to GMPPCP, GDP, AlF_4^- , and GDP. Fig. S5 shows DRP GG alignments. Fig. S6 shows further comparison of Vps1 GG and dynamin 1 GG structures. Fig. S7 shows details of the cryoEM reconstruction of full-length *C. thermophilum* Vps1 assembly bound to GMPPCP. Fig. S8 shows validation of the Stalk interfaces of the Vps1 helical assembly. Table S1 shows yeast strains used in this study. Table S2 shows cell biology-related plasmids used in this study. Table S3 shows crystallographic data collection and processing. Table S4 shows refinement. Table S5 shows model geometry. Video 1 shows vacuoles in W303A cells. Video 2 shows vacuoles in $\Delta vps1$ cells. Video 3 shows localization of GFP-FYVE in W303A cells. Video 4 shows localization of GFP-FYVE in $\Delta vps1$ cells. Video 5 shows morph between GG_{GMPPCP} and GG_{GDP} . Video 6 shows morph between GG_{GMPPCP} and GG_{GDP,AlF_4^-} .

Acknowledgments

C. thermophilum cDNA, GFP-SNC1, and GFP-TLG2 were gifts from Ed Hurt (University of Heidelberg, Heidelberg, Germany) and Allyson O'Donnell (University of Pittsburgh, Pittsburgh, PA). We thank Willam Furey, Simon Watkins, and the Center for Biological Imaging (University of Pittsburgh, Pittsburgh, PA), and we thank Yuriy Chaban and Daniel Clare at Diamond Light Source (Didcot, UK). We thank the beamline staffs at the Southeast Regional Collaborative Access Team (SER-CAT) and the Northeastern Collaborative Access Team (NE-CAT) at the Advanced Photon Source (APS). All final reflection data were collected at the SER-CAT 22-ID beamline at the APS (Argonne National Laboratory, Lemont, IL). Supporting institutions may be found at www.ser-cat.org/members.html. Preliminary data for GG_{GMPPCP} were collected on NE-CAT beamline 24-ID-C under the General User Proposal GUP-51113 (PI: J.S. Chappie), which is funded by the National Institute of General Medical Sciences from the National Institutes of Health (P41 GM103403).

The Pilatus 6M detector on the 24-ID-C beamline is funded by a National Institutes of Health Office of Research Infrastructure Programs High-End Instrumentation grant (S10 RR029205). This research used resources of the APS, a US Department of Energy (DOE) Office of Science User Facility operated for the Department of Energy Office of Science by Argonne National Laboratory under contract number DE-AC02-06CH11357. Use of the APS was supported by the US Department of Energy, Office of Science, Office of Basic Energy Sciences under contract number W-31-109-Eng-38. We acknowledge Diamond Light Source for access and support of the CryoEM facilities at the UK National Electron Bio-Imaging Centre funded by the Wellcome Trust, Medical Research Council, and Biotechnology and Biological Sciences Research Council (proposal EM14856-13). This study was supported by the National Institutes of Health (grants GM120102 to M.G.J. Ford and GM082251 to P. Zhang) and the UK Wellcome Trust Investigator Award 206422/Z/17/Z (to P. Zhang). J.S. Chappie is a Nancy and Peter Meinig Investigator in the Life Sciences.

The authors declare no competing financial interests.

Author contributions: N.V. Varlakhanova designed and performed experiments, analyzed and interpreted data, and wrote and revised the manuscript; F.J.D. Alvarez designed and performed experiments, analyzed and interpreted data, and revised the manuscript; T.M. Brady, B.A. Tornabene, and C.J. Hosford performed experiments; J.S. Chappie and P. Zhang provided conceptual advice, analyzed data, and revised the manuscript; M.G.J. Ford conceived the project, designed and performed experiments, analyzed and interpreted data, and wrote and revised the manuscript.

Submitted: 5 December 2017

Revised: 26 May 2018

Accepted: 17 July 2018

References

- Achiriloie, M., B. Barylko, and J.P. Albanesi. 1999. Essential role of the dynamin pleckstrin homology domain in receptor-mediated endocytosis. *Mol. Cell. Biol.* 19:1410–1415. <https://doi.org/10.1128/MCB.19.2.1410>
- Adams, P.D., P.V. Afonine, G. Bunkóczi, V.B. Chen, I.W. Davis, N. Echols, J.J. Headd, L.W. Hung, G.J. Kapral, R.W. Grosse-Kunstleve, et al. 2010. PHE NIX: a comprehensive Python-based system for macromolecular structure solution. *Acta Crystallogr. D Biol. Crystallogr.* 66:213–221. <https://doi.org/10.1107/S0907444909052925>
- Afonine, P.V., R.W. Grosse-Kunstleve, N. Echols, J.J. Headd, N.W. Moriarty, M. Mustyakimov, T.C. Terwilliger, A. Urzhumtsev, P.H. Zwart, and P.D. Adams. 2012. Towards automated crystallographic structure refinement with phenix.refine. *Acta Crystallogr. D Biol. Crystallogr.* 68:352–367. <https://doi.org/10.1107/S0907444912001308>
- Alvarez, F.J.D., S. He, J.R. Perilla, S. Jang, K. Schulten, A.N. Engelman, S.H.W. Scheres, and P. Zhang. 2017. CryoEM structure of MxB reveals a novel oligomerization interface critical for HIV restriction. *Sci. Adv.* 3:e1701264. <https://doi.org/10.1126/sciadv.1701264>
- Amlacher, S., P. Sarges, D. Flemming, V. van Noort, R. Kunze, D.P. Devos, M. Arumugam, P. Bork, and E. Hurt. 2011. Insight into structure and assembly of the nuclear pore complex by utilizing the genome of a eukaryotic thermophile. *Cell*. 146:277–289. <https://doi.org/10.1016/j.cell.2011.06.039>
- Anand, R., S. Eschenburg, and T.F. Reubold. 2016. Crystal structure of the GTPase domain and the bundle signalling element of dynamin in the GDP state. *Biochem. Biophys. Res. Commun.* 469:76–80. <https://doi.org/10.1016/j.bbrc.2015.11.074>
- Antonny, B., C. Burd, P. De Camilli, E. Chen, O. Daumke, K. Faelber, M. Ford, V.A. Frolov, A. Frost, J.E. Hinshaw, et al. 2016. Membrane fission by dynamin: what we know and what we need to know. *EMBO J.* 35:2270–2284. <https://doi.org/10.15252/emboj.201694613>
- Arlt, H., F. Reggiori, and C. Ungermann. 2015. Retromer and the dynamin Vps1 cooperate in the retrieval of transmembrane proteins from vacuoles. *J. Cell Sci.* 128:645–655. <https://doi.org/10.1242/jcs.132720>
- Babst, M., T.K. Sato, L.M. Banta, and S.D. Emr. 1997. Endosomal transport function in yeast requires a novel AAA-type ATPase, Vps4p. *EMBO J.* 16:1820–1831. <https://doi.org/10.1093/emboj/16.8.1820>
- Battye, T.G., L. Kontogiannis, O. Johnson, H.R. Powell, and A.G. Leslie. 2011. iMOSFLM: a new graphical interface for diffraction-image processing with MOSFLM. *Acta Crystallogr. D Biol. Crystallogr.* 67:271–281. <https://doi.org/10.1107/S0907444910048675>
- Bian, X., R.W. Klemm, T.Y. Liu, M. Zhang, S. Sun, X. Sui, X. Liu, T.A. Rapoport, and J. Hu. 2011. Structures of the atlastin GTPase provide insight into homotypic fusion of endoplasmic reticulum membranes. *Proc. Natl. Acad. Sci. USA*. 108:3976–3981. <https://doi.org/10.1073/pnas.1101643108>
- Burd, C.G., and S.D. Emr. 1998. Phosphatidylinositol(3)-phosphate signaling mediated by specific binding to RING FYVE domains. *Mol. Cell*. 2:157–162. [https://doi.org/10.1016/S1097-2765\(00\)80125-2](https://doi.org/10.1016/S1097-2765(00)80125-2)
- Byrnes, L.J., and H. Sondermann. 2011. Structural basis for the nucleotide-dependent dimerization of the large G protein atlastin-1/SPG3A. *Proc. Natl. Acad. Sci. USA*. 108:2216–2221. <https://doi.org/10.1073/pnas.1012792108>

- Byrnes, L.J., A. Singh, K. Szeto, N.M. Benveniste, J.P. O'Donnell, W.R. Zipfel, and H. Sondermann. 2013. Structural basis for conformational switching and GTP loading of the large G protein atlastin. *EMBO J.* 32:369–384. <https://doi.org/10.1038/emboj.2012.353>
- Cao, Y.L., S. Meng, Y. Chen, J.X. Feng, D.D. Gu, B. Yu, Y.J. Li, J.Y. Yang, S. Liao, D.C. Chan, and S. Gao. 2017. MFN1 structures reveal nucleotide-triggered dimerization critical for mitochondrial fusion. *Nature*. 542:372–376. <https://doi.org/10.1038/nature21077>
- Chappie, J.S., and F. Dyda. 2013. Building a fission machine—structural insights into dynamin assembly and activation. *J. Cell Sci.* 126:2773–2784. <https://doi.org/10.1242/jcs.108845>
- Chappie, J.S., S. Acharya, Y.W. Liu, M. Leonard, T.J. Pucadyil, and S.L. Schmid. 2009. An intramolecular signaling element that modulates dynamin function in vitro and in vivo. *Mol. Biol. Cell.* 20:3561–3571. <https://doi.org/10.1091/mbc.e09-04-0318>
- Chappie, J.S., S. Acharya, M. Leonard, S.L. Schmid, and F. Dyda. 2010. G domain dimerization controls dynamin's assembly-stimulated GTPase activity. *Nature*. 465:435–440. <https://doi.org/10.1038/nature09032>
- Chappie, J.S., J.A. Mears, S. Fang, M. Leonard, S.L. Schmid, R.A. Milligan, J.E. Hinshaw, and F. Dyda. 2011. A pseudoatomic model of the dynamin polymer identifies a hydrolysis-dependent powerstroke. *Cell*. 147:209–222. <https://doi.org/10.1016/j.cell.2011.09.003>
- Chi, R.J., J. Liu, M. West, J. Wang, G. Odorizzi, and C.G. Burd. 2014. Fission of SNX-BAR-coated endosomal retrograde transport carriers is promoted by the dynamin-related protein Vps1. *J. Cell Biol.* 204:793–806. <https://doi.org/10.1083/jcb.201309084>
- Collaborative Computational Project, Number 4. 1994. The CCP4 suite: programs for protein crystallography. *Acta Crystallogr. D Biol. Crystallogr.* 50:760–763. <https://doi.org/10.1107/S0907444994003112>
- Damke, H., T. Baba, D.E. Warnock, and S.L. Schmid. 1994. Induction of mutant dynamin specifically blocks endocytic coated vesicle formation. *J. Cell Biol.* 127:915–934. <https://doi.org/10.1083/jcb.127.4.915>
- Desfosses, A., R. Ciuffa, I. Gutsche, and C. Sachse. 2014. SPRING - an image processing package for single-particle based helical reconstruction from electron cryomicrographs. *J. Struct. Biol.* 185:15–26. <https://doi.org/10.1016/j.jsb.2013.11.003>
- Edgar, R.C. 2004. MUSCLE: multiple sequence alignment with high accuracy and high throughput. *Nucleic Acids Res.* 32:1792–1797. <https://doi.org/10.1093/nar/gkh340>
- Egelman, E.H. 2007. The iterative helical real space reconstruction method: surmounting the problems posed by real polymers. *J. Struct. Biol.* 157:83–94. <https://doi.org/10.1016/j.jsb.2006.05.015>
- Emsley, P., B. Lohkamp, W.G. Scott, and K. Cowtan. 2010. Features and development of Coot. *Acta Crystallogr. D Biol. Crystallogr.* 66:486–501. <https://doi.org/10.1107/S0907444910007493>
- Evans, P. 2006. Scaling and assessment of data quality. *Acta Crystallogr. D Biol. Crystallogr.* 62:72–82. <https://doi.org/10.1107/S0907444905036693>
- Faelber, K., Y. Posor, S. Gao, M. Held, Y. Roske, D. Schulze, V. Haucke, F. Noé, and O. Daumke. 2011. Crystal structure of nucleotide-free dynamin. *Nature*. 477:556–560. <https://doi.org/10.1038/nature10369>
- Faelber, K., S. Gao, M. Held, Y. Posor, V. Haucke, F. Noé, and O. Daumke. 2013. Oligomerization of dynamin superfamily proteins in health and disease. *Prog. Mol. Biol. Transl. Sci.* 117:411–443. <https://doi.org/10.1016/B978-0-12-386931-9.00015-5>
- Ferguson, S.M., and P. De Camilli. 2012. Dynamin, a membrane-remodeling GTPase. *Nat. Rev. Mol. Cell Biol.* 13:75–88. <https://doi.org/10.1038/nrm3266>
- Finken-Eigen, M., R.A. Röhrich, and K. Köhrer. 1997. The VPS4 gene is involved in protein transport out of a yeast pre-vacuolar endosome-like compartment. *Curr. Genet.* 31:469–480. <https://doi.org/10.1007/s002940050232>
- Ford, M.G., S. Jenni, and J. Nunnari. 2011. The crystal structure of dynamin. *Nature*. 477:561–566. <https://doi.org/10.1038/nature10441>
- Francy, C.A., R.W. Clinton, C. Fröhlich, C. Murphy, and J.A. Mears. 2017. Cryo-EM Studies of Drp1 Reveal Cardiolipin Interactions that Activate the Helical Oligomer. *Sci. Rep.* 7:10744. <https://doi.org/10.1038/s41598-017-11008-3>
- Fratti, R.A., Y. Jun, A.J. Merz, N. Margolis, and W. Wickner. 2004. Interdependent assembly of specific regulatory lipids and membrane fusion proteins into the vertex ring domain of docked vacuoles. *J. Cell Biol.* 167:1087–1098. <https://doi.org/10.1083/jcb.200409068>
- Fröhlich, C., S. Grabiger, D. Schwefel, K. Faelber, E. Rosenbaum, J. Mears, O. Rocks, and O. Daumke. 2013. Structural insights into oligomerization and mitochondrial remodeling of dynamin 1-like protein. *EMBO J.* 32:1280–1292. <https://doi.org/10.1038/emboj.2013.74>
- Gao, S., A. von der Malsburg, S. Paeschke, J. Behlke, O. Haller, G. Kochs, and O. Daumke. 2010. Structural basis of oligomerization in the stalk region of dynamin-like MxA. *Nature*. 465:502–506. <https://doi.org/10.1038/nature08972>
- Gao, S., A. von der Malsburg, A. Dick, K. Faelber, G.F. Schröder, O. Haller, G. Kochs, and O. Daumke. 2011. Structure of myxovirus resistance protein a reveals intra- and intermolecular domain interactions required for the antiviral function. *Immunity*. 35:514–525. <https://doi.org/10.1016/j.immuni.2011.07.012>
- Gillooly, D.J., I.C. Morrow, M. Lindsay, R. Gould, N.J. Bryant, J.M. Gaullier, R.G. Parton, and H. Stenmark. 2000. Localization of phosphatidylinositol 3-phosphate in yeast and mammalian cells. *EMBO J.* 19:4577–4588. <https://doi.org/10.1093/emboj/19.17.4577>
- Goldstein, A.L., and J.H. McCusker. 1999. Three new dominant drug resistance cassettes for gene disruption in *Saccharomyces cerevisiae*. *Yeast*. 15:1541–1553. [https://doi.org/10.1002/\(SICI\)1097-0061\(199910\)15:14%3C1541::AID-YEA476%3E3.0.CO;2-K](https://doi.org/10.1002/(SICI)1097-0061(199910)15:14%3C1541::AID-YEA476%3E3.0.CO;2-K)
- Hayden, J., M. Williams, A. Granich, H. Ahn, B. Tenay, J. Lukehart, C. Highfill, S. Dobard, and K. Kim. 2013. Vps1 in the late endosome-to-vacuole traffic. *J. Biosci.* 38:73–83. <https://doi.org/10.1007/s12038-012-9295-2>
- He, S., and S.H.W. Scheres. 2017. Helical reconstruction in RELION. *J. Struct. Biol.* 198:163–176. <https://doi.org/10.1016/j.jsb.2017.02.003>
- Hoppins, S., L. Lackner, and J. Nunnari. 2007. The machines that divide and fuse mitochondria. *Annu. Rev. Biochem.* 76:751–780. <https://doi.org/10.1146/annurev.biochem.76.071905.090048>
- Ingerman, E., and J. Nunnari. 2005. A continuous, regenerative coupled GTPase assay for dynamin-related proteins. *Methods Enzymol.* 404:611–619. [https://doi.org/10.1016/S0076-6879\(05\)04053-X](https://doi.org/10.1016/S0076-6879(05)04053-X)
- Ingerman, E., E.M. Perkins, M. Marino, J.A. Mears, J.M. McCaffery, J.E. Hinshaw, and J. Nunnari. 2005. Dnm1 forms spirals that are structurally tailored to fit mitochondria. *J. Cell Biol.* 170:1021–1027. <https://doi.org/10.1083/jcb.200506078>
- Kenniston, J.A., and M.A. Lemmon. 2010. Dynamin GTPase regulation is altered by PH domain mutations found in centronuclear myopathy patients. *EMBO J.* 29:3054–3067. <https://doi.org/10.1038/emboj.2010.187>
- Kuravi, K., S. Nagotu, A.M. Krikken, K. Sjölema, M. Deckers, R. Erdmann, M. Veenhuis, and I.J. van der Klei. 2006. Dynamin-related proteins Vps1p and Dnm1p control peroxisome abundance in *Saccharomyces cerevisiae*. *J. Cell Sci.* 119:3994–4001. <https://doi.org/10.1242/jcs.03166>
- Leonard, M., B.D. Song, R. Ramachandran, and S.L. Schmid. 2005. Robust colorimetric assays for dynamin's basal and stimulated GTPase activities. *Methods Enzymol.* 404:490–503. [https://doi.org/10.1016/S0076-6879\(05\)04043-7](https://doi.org/10.1016/S0076-6879(05)04043-7)
- Lewis, M.J., B.J. Nichols, C. Prescianotto-Baschong, H. Riezman, and H.R. Pelham. 2000. Specific retrieval of the exocytic SNARE Snc1p from early yeast endosomes. *Mol. Biol. Cell.* 11:23–38. <https://doi.org/10.1091/mbc.11.1.23>
- Longtine, M.S., A. McKenzie III, D.J. Demarini, N.G. Shah, A. Wach, A. Brachat, P. Philippsen, and J.R. Pringle. 1998. Additional modules for versatile and economical PCR-based gene deletion and modification in *Saccharomyces cerevisiae*. *Yeast*. 14:953–961. [https://doi.org/10.1002/\(SICI\)1097-0061\(199807\)14:10%3C953::AID-YEA293%3E3.0.CO;2-U](https://doi.org/10.1002/(SICI)1097-0061(199807)14:10%3C953::AID-YEA293%3E3.0.CO;2-U)
- Low, H.H., and J. Löwe. 2006. A bacterial dynamin-like protein. *Nature*. 444:766–769. <https://doi.org/10.1038/nature05312>
- Low, H.H., C. Sachse, L.A. Amos, and J. Löwe. 2009. Structure of a bacterial dynamin-like protein lipid tube provides a mechanism for assembly and membrane curving. *Cell*. 139:1342–1352. <https://doi.org/10.1016/j.cell.2009.11.003>
- Lukehart, J., C. Highfill, and K. Kim. 2013. Vps1, a recycling factor for the traffic from early endosome to the late Golgi. *Biochem. Cell Biol.* 91:455–465. <https://doi.org/10.1139/bcb-2013-0044>
- McCoy, A.J., R.W. Grosse-Kunstleve, P.D. Adams, M.D. Winn, L.C. Storoni, and R.J. Read. 2007. Phaser crystallographic software. *J. Appl. Cryst.* 40:658–674. <https://doi.org/10.1107/S0021889807021206>
- Millen, J.L., R. Krick, T. Prick, M. Thumm, and D.S. Goldfarb. 2009. Measuring piecemeal microautophagy of the nucleus in *Saccharomyces cerevisiae*. *Autophagy*. 5:75–81. <https://doi.org/10.4161/auto.5.1.7181>
- Peters, C., T.L. Baars, S. Bühler, and A. Mayer. 2004. Mutual control of membrane fission and fusion proteins. *Cell*. 119:667–678. <https://doi.org/10.1016/j.cell.2004.11.023>
- Pettersen, E.F., T.D. Goddard, C.C. Huang, G.S. Couch, D.M. Greenblatt, E.C. Meng, and T.E. Ferrin. 2004. UCSF Chimera—a visualization system for exploratory research and analysis. *J. Comput. Chem.* 25:1605–1612. <https://doi.org/10.1002/jcc.20084>

- Praefcke, G.J., and H.T. McMahon. 2004. The dynamin superfamily: universal membrane tubulation and fission molecules? *Nat. Rev. Mol. Cell Biol.* 5:133–147. <https://doi.org/10.1038/nrml1313>
- Qi, Y., L. Yan, C. Yu, X. Guo, X. Zhou, X. Hu, X. Huang, Z. Rao, Z. Lou, and J. Hu. 2016. Structures of human mitofusin 1 provide insight into mitochondrial tethering. *J. Cell Biol.* 215:621–629. <https://doi.org/10.1083/jcb.201609019>
- Ramachandran, R., T.J. Pucadyil, Y.W. Liu, S. Acharya, M. Leonard, V. Lukiyanchuk, and S.L. Schmid. 2009. Membrane insertion of the pleckstrin homology domain variable loop 1 is critical for dynamin-catalyzed vesicle scission. *Mol. Biol. Cell.* 20:4630–4639. <https://doi.org/10.1091/mbc.e09-08-0683>
- Raymond, C.K., I. Howald-Stevenson, C.A. Vater, and T.H. Stevens. 1992. Morphological classification of the yeast vacuolar protein sorting mutants: evidence for a prevacuolar compartment in class E vps mutants. *Mol. Biol. Cell.* 3:1389–1402. <https://doi.org/10.1091/mbc.3.12.1389>
- Reubold, T.F., K. Faelber, N. Plattner, Y. Posor, K. Ketel, U. Curth, J. Schlegel, R. Anand, D.J. Manstein, F. Noé, et al. 2015. Crystal structure of the dynamin tetramer. *Nature.* 525:404–408. <https://doi.org/10.1038/nature14880>
- Robert, X., and P. Gouet. 2014. Deciphering key features in protein structures with the new ENDscript server. *Nucleic Acids Res.* 42(W1):W320–W324. <https://doi.org/10.1093/nar/gku316>
- Rohou, A., and N. Grigorieff. 2015. CTFFIND4: Fast and accurate defocus estimation from electron micrographs. *J. Struct. Biol.* 192:216–221. <https://doi.org/10.1016/j.jsb.2015.08.008>
- Rothman, J.H., and T.H. Stevens. 1986. Protein sorting in yeast: mutants defective in vacuole biogenesis mislocalize vacuolar proteins into the late secretory pathway. *Cell.* 47:1041–1051. [https://doi.org/10.1016/0092-8674\(86\)90819-6](https://doi.org/10.1016/0092-8674(86)90819-6)
- Rothman, J.H., C.K. Raymond, T. Gilbert, P.J. O'Hara, and T.H. Stevens. 1990. A putative GTP binding protein homologous to interferon-inducible Mx proteins performs an essential function in yeast protein sorting. *Cell.* 61:1063–1074. [https://doi.org/10.1016/0092-8674\(90\)90070-U](https://doi.org/10.1016/0092-8674(90)90070-U)
- Saimani, U., J. Smothers, H. McDermott, P. Makaraci, and K. Kim. 2017. Yeast dynamin associates with the GARP tethering complex for endosome-to-Golgi traffic. *Eur. J. Cell Biol.* 96:612–621. <https://doi.org/10.1016/j.ejcb.2017.04.004>
- Schindelin, J., I. Arganda-Carreras, E. Frise, V. Kaynig, M. Longair, T. Pietzsch, S. Preibisch, C. Rueden, S. Saalfeld, B. Schmid, et al. 2012. Fiji: an open-source platform for biological-image analysis. *Nat. Methods.* 9:676–682. <https://doi.org/10.1038/nmeth.2019>
- Schöneberg, J., I.H. Lee, J.H. Iwasa, and J.H. Hurley. 2017. Reverse-topology membrane scission by the ESCRT proteins. *Nat. Rev. Mol. Cell Biol.* 18:5–17. <https://doi.org/10.1038/nrm.2016.121>
- Shaikh, T.R., H. Gao, W.T. Baxter, F.J. Asturias, N. Boisset, A. Leith, and J. Frank. 2008. SPIDER image processing for single-particle reconstruction of biological macromolecules from electron micrographs. *Nat. Protoc.* 3:1941–1974. <https://doi.org/10.1038/nprot.2008.156>
- Shestakova, A., A. Hanono, S. Drosner, M. Curtiss, B.A. Davies, D.J. Katzmman, and M. Babst. 2010. Assembly of the AAA ATPase Vps4 on ESCRT-III. *Mol. Biol. Cell.* 21:1059–1071. <https://doi.org/10.1091/mbc.e09-07-0572>
- Smaczynska-de Rooij, I.I., E.G. Allwood, S. Aghamohammadzadeh, E.H. Hetttema, M.W. Goldberg, and K.R. Ayscough. 2010. A role for the dynamin-like protein Vps1 during endocytosis in yeast. *J. Cell Sci.* 123:3496–3506. <https://doi.org/10.1242/jcs.070508>
- Smaczynska-de Rooij, I.I., E.G. Allwood, R. Mishra, W.I. Booth, S. Aghamohammadzadeh, M.W. Goldberg, and K.R. Ayscough. 2012. Yeast dynamin Vps1 and amphiphysin Rvs167 function together during endocytosis. *Traffic.* 13:317–328. <https://doi.org/10.1111/j.1600-0854.2011.01311.x>
- Stevens, T., B. Esmon, and R. Schekman. 1982. Early stages in the yeast secretory pathway are required for transport of carboxypeptidase Y to the vacuole. *Cell.* 30:439–448. [https://doi.org/10.1016/0092-8674\(82\)90241-0](https://doi.org/10.1016/0092-8674(82)90241-0)
- Stowell, M.H., B. Marks, P. Wigge, and H.T. McMahon. 1999. Nucleotide-dependent conformational changes in dynamin: evidence for a mechanochemical molecular spring. *Nat. Cell Biol.* 1:27–32. <https://doi.org/10.1038/8997>
- Sundborger, A.C., S. Fang, J.A. Heymann, P. Ray, J.S. Chappie, and J.E. Hinshaw. 2014. A dynamin mutant defines a superconstricted pre-fission state. *Cell Reports.* 8:734–742. <https://doi.org/10.1016/j.celrep.2014.06.054>
- Tang, G., L. Peng, P.R. Baldwin, D.S. Mann, W. Jiang, I. Rees, and S.J. Ludtke. 2007. EMAN2: an extensible image processing suite for electron microscopy. *J. Struct. Biol.* 157:38–46. <https://doi.org/10.1016/j.jsb.2006.05.009>
- Vater, C.A., C.K. Raymond, K. Ekena, I. Howald-Stevenson, and T.H. Stevens. 1992. The VPS1 protein, a homolog of dynamin required for vacuolar protein sorting in *Saccharomyces cerevisiae*, is a GTPase with two functionally separable domains. *J. Cell Biol.* 119:773–786. <https://doi.org/10.1083/jcb.119.4.773>
- Vida, T.A., and S.D. Emr. 1995. A new vital stain for visualizing vacuolar membrane dynamics and endocytosis in yeast. *J. Cell Biol.* 128:779–792. <https://doi.org/10.1083/jcb.128.5.779>
- Warnock, D.E., L.J. Terlecky, and S.L. Schmid. 1995. Dynamin GTPase is stimulated by crosslinking through the C-terminal proline-rich domain. *EMBO J.* 14:1322–1328.
- Yan, L., Y. Ma, Y. Sun, J. Gao, X. Chen, J. Liu, C. Wang, Z. Rao, and Z. Lou. 2011. Structural basis for mechanochemical role of Arabidopsis thaliana dynamin-related protein in membrane fission. *J. Mol. Cell Biol.* 3:378–381. <https://doi.org/10.1093/jmcb/mjr032>
- Zheng, S.Q., E. Palovcak, J.-P. Armache, Y. Cheng, and D.A. Agard. 2017. MotionCor2 - anisotropic correction of beam-induced motion for improved cryo-electron microscopy. *Nature methods.* 14:331–332. <https://doi.org/10.1038/nmeth.4193>